Summer 2014

WRF-Model Data Assimilation Studies of Landfalling Atmospheric Rivers and Orographic Precipitation Over Northern California

Arthur John Eiserloh
San Jose State University

WRF-MODEL DATA ASSIMILATION STUDIES OF LANDFALLING ATMOSPHERIC RIVERS AND OROGRAPHIC PRECIPITATION OVER NORTHERN CALIFORNIA

A Thesis

Presented to

The Faculty of the Department of Meteorology and Climate Science

San José State University

In Partial Fulfillment

of the Requirements for the Degree

Masters of Science

by

Arthur J. Eiserloh, Jr.

August 2014

The Designated Thesis Committee Approves the Thesis Titled

WRF-MODEL DATA ASSIMILATION STUDIES OF LANDFALLING ATMOSPHERIC RIVERS AND OROGRAPHIC PRECIPITATION OVER NORTHERN CALIFORNIA

by

Arthur J. Eiserloh Jr.

APPROVED FOR THE DEPARTMENT OF METEOROLOGY AND CLIMATE SCIENCE

SAN JOSÉ STATE UNIVERSITY

August 2014

Dr. Sen Chiao	Department of Meteorology and Climate Science
Dr. Craig Clements	Department of Meteorology and Climate Science
Dr. Marty Leach	Department of Meteorology and Climate Science

ABSTRACT

WRF-MODEL DATA ASSIMILATION STUDIES OF LANDFALLING ATMOSPHERIC RIVERS AND OROGRAPHIC PRECIPITATION OVER NORTHERN CALIFORNIA

by Arthur J. Eiserloh Jr.

In this study, data assimilation methods of 3-D variational analysis (3DVAR), observation nudging, and analysis (grid) nudging were evaluated in the Weather Research and Forecasting (WRF) model for a high-impact, multi-episode landfalling atmospheric river (AR) event for Northern California from 28 November to 3 December, 2012. Eight experiments were designed to explore various combinations of the data assimilation methods and different initial conditions. The short-to-medium range quantitative precipitation forecast (QPF) performances were tested for each experiment. Surface observations from the National Oceanic and Atmospheric Administration's (NOAA) Hydrometeorology Network (HMT), National Weather Service (NWS) radiosondes, and GPS Radio Occultation (RO) vertical profiles from the Constellation Observing System for Meteorology Ionosphere and Climate (COSMIC) satellites were used for assimilation. Model results 2.5 days into the forecast showed slower timing of the 2nd AR episode by a few hours and an underestimation in AR strength. For the entire event forecasts, the non-grid-nudging experiments showed the lowest mean absolute error (MAE) for rainfall accumulations, especially those with 3DVAR. Higher-resolution initial conditions showed more realistic coastal QPFs. Also, a 3-h nudging time interval and time window for observation nudging and 3DVAR, respectively, may be too large for this type of event, and it did not show skill until 60-66 h into the forecast.

ACKNOWLEDGEMENTS

I want to acknowledge my advisor, Dr. Sen Chiao, for all of his endless support and advice. None of this would have been possible without him. He had an open-door policy, and he always made time to assist me even if he was busy teaching classes, helping his other graduate and undergraduate students, and doing his own research. I am forever grateful for all of his encouragement and push to give an oral presentation at the annual American Meteorological Society conference. I would also like to thank my committee members, Dr. Craig Clements and Dr. Marty Leach, for their edits and advice.

I want to thank Timothy Coleman from NOAA's ESRL for assistance with the HMT dataset, Cindy Bruyere from UCAR in assistance with the WRF data assimilation methods, and the other suppliers of the data used. This research was supported via Dr. Chiao from the Grant W911NF-09-1-0441 from the U.S. Army Research Office.

I would like to thank my family, my girlfriend and her family, and my friends in San José (a.k.a. "The Family"). Throughout my graduate school experience, they always supported me mentally and emotionally no matter what. I am extremely grateful for all of my classmates at San José State, especially Diana Centeno and Braniff Davis. Diana gave me mental support and always reminded me of important deadlines, while Braniff helped me with GIS. Also, I thank all of my professors at San José State, the whole Meteorology and Climate Science Department, and especially the department chair, Dr. Alison Bridger.

TABLE OF CONTENTS

LIST OF TABLES

LIST OF FIGURES

1. Introduction

California receives most of its rainfall during its cool season when mid-latitude (ML) cyclones track farther south into the northeastern Pacific Ocean. The warm sector within these ML cyclones includes a low-level jet (LLJ) that is responsible for transporting large amounts of heat and moisture from the tropics to the mid-latitudes. These relatively thin warm-conveyor belts of heat and moisture transport are known as "atmospheric rivers" (ARs) (Newell et al. 1992). They are responsible for more than ninety percent of the atmosphere's meridional moisture transport at any given time (Zhu and Newell 1998; Ralph et al. 2004). Most ARs affect California during the cool season (October through March) and tap heat and moisture directly from the tropics (Neiman et al. 2008). Ralph et al. (2004) classify ARs as having a narrower width (< 1000 km) relative to their length (> 2000 km) and observed vertically integrated water vapor (IWV) values greater than or equal to 2 cm. The majority (~75%) of the horizontal water vapor transport in ARs exists below 2.25 km., and the LLJs within these ARs rest about 1 km above the ocean surface and usually have a maximum jet strength greater than 20 ms^{-1} (Ralph et al. 2005).

Landfalling ARs are extremely important for California's water resources, but they can also cause dangerous flooding. Previous studies have documented the connection between landfalling ARs and flooding events along the U.S. West Coast (Ralph et al. 2003, 2006; Neiman et al. 2011). Millions of dollars in property damage can occur as a result from this type of flood event (Neiman et al. 2002). Although they can cause flooding, ARs are also responsible for twenty-five to fifty percent of California's

annual precipitation (Dettinger et al. 2011). Ralph and Dettinger (2012) found that almost all 3-day precipitation events from 1997 to 2008 that were greater than 400 mm happened in California, Texas, or the Southeastern U.S. Also, they found that from 1950 to 2008, more than ninety-one percent of 3-day precipitation events that were greater 400 mm in the western U.S. occurred simultaneously with a landfalling AR. Thus, they are vital for California and are an important connection between California's weather and climate.

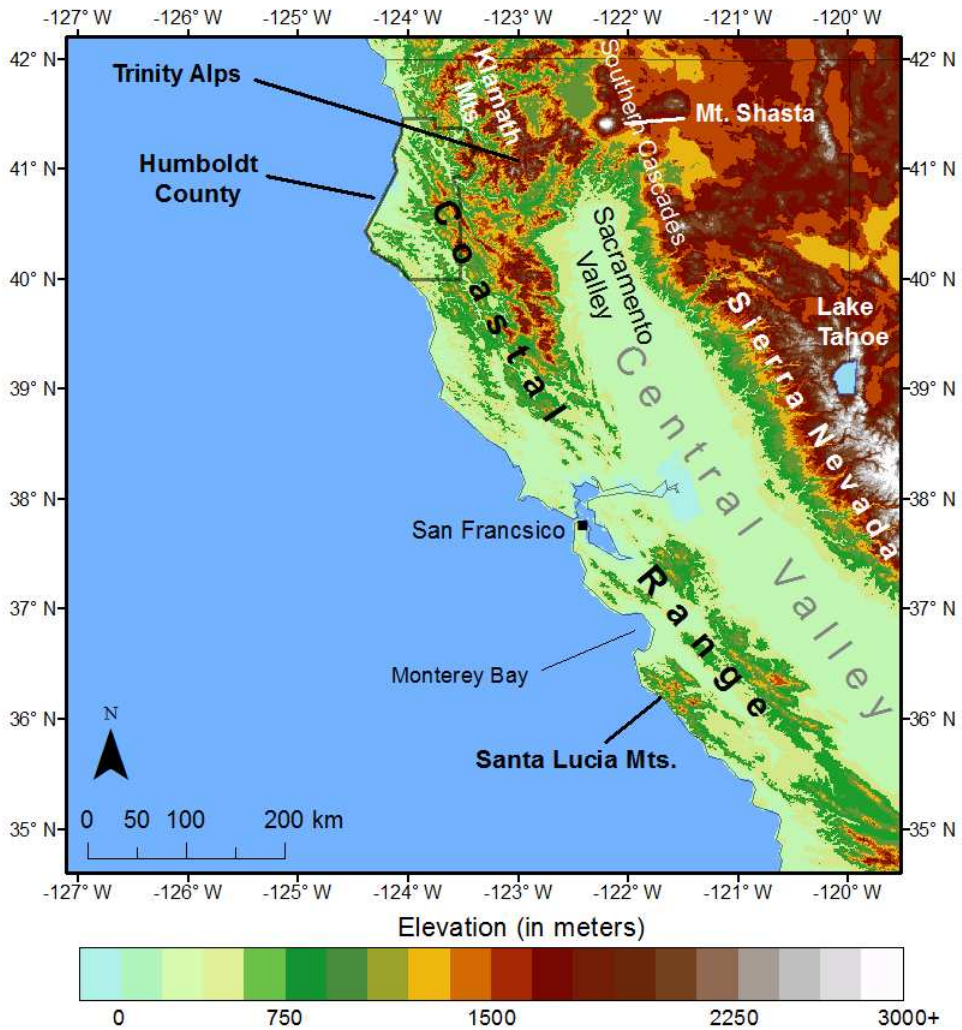

FIG. 1. Geographical features of interest in this study over Northern California.

Orographically enhanced precipitation is the primary mechanism that causes flooding from landfalling ARs and winter storms along the windward slopes of California's mountain ranges (Fig. 1). The strength of orographic precipitation depends on a variety of variables including terrain height, upstream moisture content, impinging wind speed and direction, and slope steepness (Lin et al. 2001; Neiman et al. 2002; Ralph et al. 2003). Along the Coastal Range (mountain heights ~500-2200 MSL), Neiman et al. (2002) found strong correlation coefficients (> 0.7) between the wind speed perpendicular to the mountains and the magnitude of hourly rainfall rates, with the highest correlations near the height of the LLJ (~ 1 km). Ralph et al. (2003) showed that wind differences of only 10 degrees can put a river basin either in the direct path of the strongest orographic rainfall rates or in a rain shadow. If the onshore flow has some degree of stability but is forced to rise over the quasi-linear northwest-southeast Sierra Nevada and Coastal Range, then blocked flows and barrier jets (e.g., Sierra Barrier Jet and Coastal Barrier Jet) can form at the base of the mountains. These processes can redistribute rainfall maxima and cause frontal modifications (Marwitz 1987; Neiman et al. 2004; Reeves et al. 2008; Smith et al. 2010; Hughes et al. 2012; Kingsmill et al. 2013). These multiple dependencies on orographic precipitation strength and duration can make mesoscale short-to-medium range [i.e., 12-240 h (World Meteorological Organization 2010)] quantitative precipitation forecasts (QPFs) for California during high-impact AR events extremely challenging.

Higher resolution mesoscale models such as the Weather Research and Forecasting (WRF) model show increased skill in terms of QPF spatial distributions for

orographic rainfall events; however, they still overestimate rainfall on windward slopes and underestimate it on the lee slopes (Colle and Mass, 2000). For landfalling winter storms on the West Coast, WRF has a positive moisture bias upstream (Hahn and Mass 2009; Ma et al. 2011) overpredicting orographic precipitation (Garvert et al., 2005). WRF also has wintertime wet bias in both short- and long-term forecasts (Chin et al. 2010).

On the improvement of QPFs in mountainous regions, Richard et al. (2005) suggested that increased efforts for mesoscale assimilation of the initial data for high-resolution numerical weather prediction and more studies on the predictability of convection and precipitation are needed. Although there have been numerous studies on WRF's performance during West Coast winter storms, there are not many WRF data assimilation studies investigating potential ways to improve orographic rainfall forecasting for California during high-impact, multi-day AR events. Recently, Ma et al. (2011) assimilated satellite GPS Radio Occultation (RO) soundings into WRF using the three-dimensional variational method (3DVAR) during a landfalling AR in the Pacific Northwest. In doing so, they slightly improved the representation of the offshore moisture profile for a 24-h forecast, specifically in the lower levels. Unfortunately, they did not further evaluate the potential QPF improvement. No studies have compared WRF data assimilation methods of 3DVAR and Four-Dimensional Data Assimilation (FDDA) methods of observation and/or analysis nudging during AR events in terms of QPFs for Northern California.

The goal of this study is to advance our understanding of orographic rainfall along the U.S. West Coast. The performance of various WRF data assimilation methods including 3DVAR, observation nudging, grid nudging and combinations of those are evaluated on their short-to-medium range QPFs during a high-impact, multi-day AR event for Northern California from 28 November to 03 December 2012. During this event, four separate ARs or "episodes" affected California in less than six days. The discussion of most results in this paper will focus on the second AR episode, Episode 2, which showed the highest 6- and 12-h rainfall rates. The data assimilation methods used the National Oceanic and Atmospheric Administration (NOAA)'s Hydrometeorology Testbed (HMT) surface stations and Constellation Observing System for Meteorology Ionosphere and Climate (COSMIC) satellite GPS RO soundings in an attempt to improve initial conditions. The hypothesis for this study was that the WRF simulations using 3DVAR with COSMIC profiles will produce more reliable representations of the ARs and more accurate QPFs because 3DVAR for WRF can include COSMIC GPS RO vertical profiles for added moisture observations upstream in the Pacific. In Section 2, data used for the event analysis and assimilation are described. The WRF experimental designs are described followed by an explanation of the data assimilation methods of FDDA nudging and 3DVAR in Section 3. The synoptic and mesoscale overview of the AR event is given in Section 4. Nested model outcomes and results of eight numerical experiments are evaluated in Section 5, concluding with a summary in Section 6.

2. Data and Analysis Methods

NOAA's HMT-West surface station network, originally established in California in the late 1990s to help improve short-term forecasting (i.e., 12-72 h) of landfalling West Coast winter storms (NOAA 2014), provided surface data for this study. The HMT goal includes collecting data for research on floods and other heavy precipitation events that are hydrological threats in water basins and river sheds. All available HMT-West surface stations in California surface weather stations (data downloaded from ftp://ftp1.esrl.noaa.gov/psd2/data/) were used for both assimilation purposes and for observation analyses. HMT surface variables available for assimilation include 2-m air temperature, relative humidity, and 10-m horizontal wind speed and direction (See Appendix B). Not all stations used for this study were equipped with rain gauges, and many stations with rain gauges showed inaccurate rainfall observations. Rainfall observations from these surface stations were also used for comparison with simulation QPFs in this study. Model experiment performance was evaluated by calculating the mean absolute error (MAE) with the HMT surface sites with the following equation:

$$MAE = \frac{1}{n}\sum_{i=1}^{n}\left| f_i - y_i \right| \quad , \qquad (1)$$

where *n* represents the number of forecasts hours, f is the model's forecasted value, and *y* is the observed value. In addition, observations from available upper air soundings from the National Weather Service (NWS) rawinsonde network were used as extra assimilation data (See Appendix B).

In an attempt to improve upstream moisture fields, COSMIC GPS RO soundings were included in some of the assimilation experiments. COSMIC (COSMIC-1/FORMOSAT-3) is a 2006 U.S./Taiwan joint mission that provides ~1500-2000 vertical soundings daily around the globe (Anthes et al. 2008). These soundings are generally scattered randomly across the globe. Out of all satellite missions that provide global GPS RO soundings (e.g., CHAMP and GPS/MET), COSMIC is the only one to provide data within the study area and time of interest. There are many benefits in using COSMIC GPS RO soundings. They are minimally affected by aerosols and precipitation, and they are not affected by instrument drift (Cucurull et al. 2007). Also, most soundings (90%) are able to get data below 1 km (Anthes et al. 2008). All soundings were downloaded in the "wetPrf" format from the COSMIC Data Analysis and Archive Center (CDAAC) (cdaac-www.cosmic.ucar.edu/cdaac/index.html). The wetPrf soundings have a vertical resolution near 100 m in the lower troposphere (Wick et al. 2008).

An observational analysis and validation of the strength and location of the AR along with the spatial distributions of rainfall accumulations was performed using vertical IWV data from the Special Sensor Microwave Imager Sounder (SSMIS) and Stage IV 6-h gridded rainfall data from the National Centers for Environmental Prediction (NCEP). SSMIS is a passively conically scanning microwave radiometer with a ground swath of approximately 1700 km and a grid size of 25 km (Northrop Grumman 2002). The SSMIS water vapor retrieval algorithm has difficulty in areas with heavy rainfall, and SSMIS itself has limited spatial and temporal resolution (Wentz 1997). In addition to SSMIS, upper-level synoptic analyses from the North American Regional Reanalysis

(NARR) dataset were studied for the AR event. NARR has a horizontal resolution of 32 km, a temporal resolution of 3 h, and a vertical resolution of 29 vertical pressure levels.

All simulated QPFs in this study were compared with NCEP's Stage IV precipitation analyses. NCEP Stage IV is a regional multi-sensor precipitation estimate of accumulated rainfall data composed of both observations from rain gauge data and radar derived quantities (Baldwin and Mitchell 1996). The data were quality controlled manually by each NWS River Forecast Center before being gridded onto a 4 km resolution grid. Inaccuracies in NCEP stage IV data exist in mountainous regions due to lack of rain gauges, radar echo blockage from the mountains, and not enough radar coverage (Jankov et al. 2007).

3. WRF Model Configuration and Experimental Designs

3.1. WRF Model Configuration

Experiments for this study were conducted with the Advanced Research WRF (WRF-ARW) model version 3.4 (Skamarock et al. 2008). WRF-ARW is 3-D, non-hydrostatic, and fully compressible with a terrain-following sigma coordinate system. All experiments were initialized at 0000 UTC 28 November 2012 and run for 138 h until the end of the AR event at 1800 UTC 03 December. They were configured with a nested grid system including an outer and inner domain (Fig. 2). Horizontal resolutions of 12 and 3 km were chosen for the outer (D1) and inner (D2) domains, respectively. The domains were positioned as such to include as many upstream COSMIC sounding locations over the ocean as possible. Both domains have a vertical resolution of 51 levels. Because it was configured with an even parent-grid ratio, feedback was turned off. The Thompson graupel (2-moment) microphysics scheme (Thompson et al. 2004) as well as the YSU boundary layer scheme (Hong et al. 2006) were used. The Thompson microphysics scheme was used because it has been found to produce a smaller wet-bias in cold season QPFs over areas of Northern California than other available microphysics options in WRF (Jankov et al. 2007). All experiments in this study, except one, used the GFS 0.5 degree forecast model (~55 km horizontal resolution) for initial conditions and boundary conditions, and the other used the ECMWF Reanalysis (ERA)-Interim [~79 km horizontal resolution (Dee et al. 2011)].

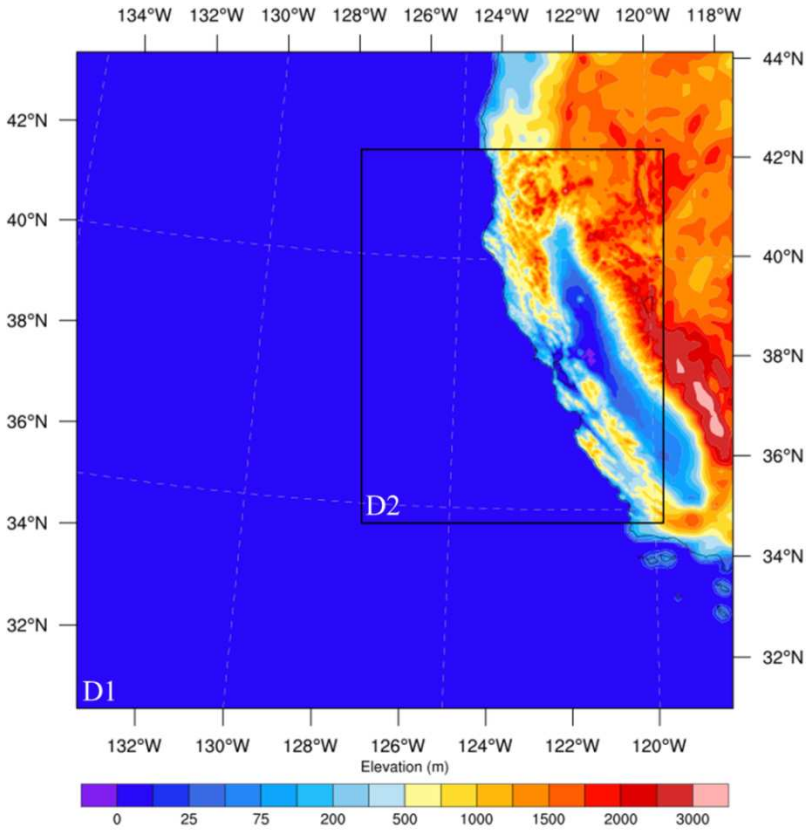

FIG. 2. Outer (D1) and inner (D2) domains used for the WRF experiments.

3.2. Data Assimilation Methods

This study used the two FDDA nudging methods, observation nudging and grid nudging, and 3DVAR (Liu et al. 2005; Barker et al. 2004) for data assimilation. Each experiment used either one or a combination of those to test which of the three methods results in more accurate QPFs during a high-impact AR event for California. Also, this study attempted to determine if it is advantageous to combine these methods. The methods in this paper are similar to the methods discussed in Yu et al. (2007). Nudging is an empirical data assimilation method, whereas 3DVAR is a statistical method (Huang 2014). FDDA nudging methods have been found to show better results for short-term

forecasts (0-12 h) (Yu et al. 2007). 3DVAR methods that use satellite data have been preferred for short-to-medium range forecasting particularly for tropical cyclone tracks (Routray et al. 2012).

3.2.1. FDDA Nudging

Nudging (i.e. "Newtonian Relaxation") relaxes the model's grid toward the observations over time by introducing artificial variables and weighting terms into the prognostic equations (Stauffer and Seaman 1994). Stauffer and Seaman (1994) explain two ways this can be achieved: 1) nudging the model's grid points directly to near-continuous observations that can be spatially and temporally non-uniform (i.e. observation nudging), and 2) nudging the model toward a gridded analysis from synoptic observations which must be time-interpolated to match the model's time step (i.e. "grid" nudging).

Observation nudging can be used for all types of observations, but it is better for continuous data assimilation of asynoptic observations like surface data, wind profilers, sodars, etc. Observation nudging only uses the observations that are within a user-defined nudging time window. Equation (2) below (Stauffer and Seaman 1994) shows how the observation nudging process is implemented into WRF:

$$\frac{\partial p^{*}\alpha}{\partial t} = F\left(\alpha, \mathbf{x}, t\right) + G_{\alpha} p^{*} \frac{\left[\sum_{i=1}^{N} W^{2}\left(\mathbf{x}, t\right) \gamma_{i} \left(\alpha_{0} - \hat{\alpha}\right)_{i}\right]}{\sum_{i=1}^{N} W_{i}\left(\mathbf{x}, t\right)}, \qquad (2)$$

where p^{*} is the flux form of pressure; α represents one of the variables that may be nudged (temperature, horizontal winds, or water vapor mixing ratio); F represents all of the model's physical forcing terms; G_{α} is the nudging factor; W is the weighting function

($W = w_{xy}w_{\sigma}w_t$) that has horizontal, vertical, and time weights; γ_i is the observational quality factor that ranges from 0 to 1; α_0 is the actual observed value; and $\hat{\alpha}$ is the model's 3-D interpolated value. The horizontal weighting function (w_{xy}) is defined as a Cressman function that depends on a user-defined horizontal radius of influence (RIN_{xy}) and the distance between the observation and model grid point. The second term on the right-hand side of equation (2) is called the observation nudging term. Over model integration time, artificial adjustments are made to the model grid points by applying a weighted average of the differences from all the observations within the RIN_{xy}. The nudging factor, $G_{\alpha,}$ is what determines the relative strength of the nudging for each nudging variable, α. Figure 3 shows what observation nudging looks like after Dudhia (2014). The circles represent the extent of the user-defined RIN_{xy} around the observations (circles), and only a few observations may be close enough to affect the model grid point (square).

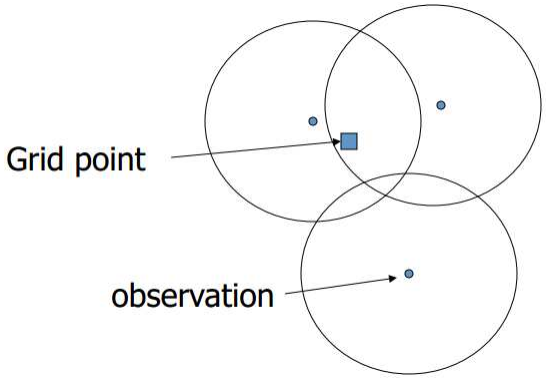

FIG. 3. Schematic illustrating observation nudging after Dudhia (2014). The circles extending from the dots represent the radii of influence and the square represents a model grid point.

Analysis nudging is a slightly simpler form of equation (1) and does not depend on a RIN_{xy}. Equation (3) (Stauffer and Seaman 1994) is how analysis nudging is accomplished in WRF:

$$\frac{\partial p^{*}\alpha}{\partial t} = F\left(\alpha, \mathbf{x}, t\right) + G_{\alpha} W(\mathbf{x}, t)\varepsilon(\mathbf{x}) p^{*}(\hat{\alpha}_{0} - \alpha), \qquad (3)$$

where most of the terms are defined similarly as in observation nudging but instead apply to the gridded analyses from observations, and $\varepsilon(\mathbf{x})$ is the gridded analysis quality factor that ranges from 0 to 1. WRF allows both forms of nudging to be applied to all nested domains. Observation files for nudging purposes in this project were created from the OBSGRID program for WRF.

3.2.2. 3DVAR

3DVAR is a data assimilation method used in mesoscale numerical weather prediction in order to produce the best estimate of the atmospheric state at any given analysis time by iteratively reducing a prescribed quadratic cost-function,

$$J(x) = J^{b} + J^{o} = \frac{1}{2}(x - x^{b})^{T} B^{-1}(x - x^{b}) + \frac{1}{2}(y - y^{o})^{T} (\mathrm{R})^{-1}(y - y^{o}) \ , \qquad (4)$$

(Barker et al. 2004). J^{b} is the background term, J^{o} is the observation term, x represents any given analysis state, x^{b} represents the background or previous forecast, y represents a separate procedure for transforming the analysis into observational space in order to compare analysis against observations, y^{o} represents the observations within a given time window, and B and R represent the background and observation error covariance matrices, respectively. Through this iteration, the analysis state, x, that provides the

minimum cost function, $J(x)$, represents the most likely estimate of the analysis solution with the least amount of variance between the observations and the background error from previous model forecasts (Barker et al. 2004). This cost function assumes that the covariances of the background error and observations are statistically described with Gaussian probability density functions with no mean error. 3DVAR is run in WRF via the WRF Data Assimilation package (WRFDA). Figure 4 demonstrates the flow of how 3DVAR works in conjunction with WRF, and Figure 5 shows the various inner-details of 3DVAR with its minimization loop of the cost-function.

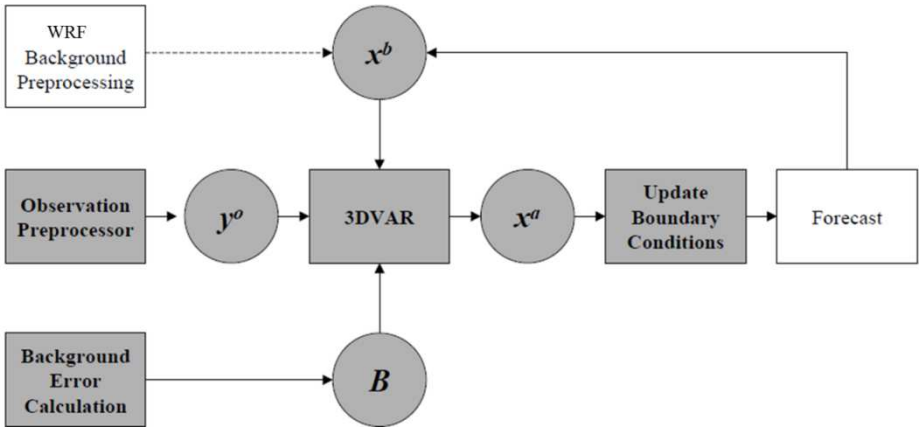

FIG. 4. Flow chart after Barker et al. (2004) of how 3DVAR is operated within WRF, where x^b, x^a, y^o, and B represent the initial background analysis, final 3DVAR updated analysis, observations, and the background error, respectively.

Three elements are needed for 3DVAR simulations: 1) the background analysis for input into WRFDA, 2) observation datasets (i.e. asynoptic data), and 3) the background error covariance statistical analysis. 3DVAR will incorporate those extra datasets to produce updated initial and time-dependent lateral boundary conditions for ingest into WRF. 3DVAR can be executed in either cold-start mode or cycling mode.

For cold-start simulations, WRF takes the newly generated background analysis from 3DVAR only at the forecast starting time and allows WRF to generate the rest of the forecast. Cycling mode uses the forecasts generated from WRF after a certain time (e.g., 3 h in this study) as new input background files for 3DVAR instead of the normal background analysis produced from previous weather forecasting models. Cycling mode requires lower boundary conditions to be updated on the newly generated analysis before proceeding with the forecast. This cyclic process continues as long as needed with the aforementioned time interval.

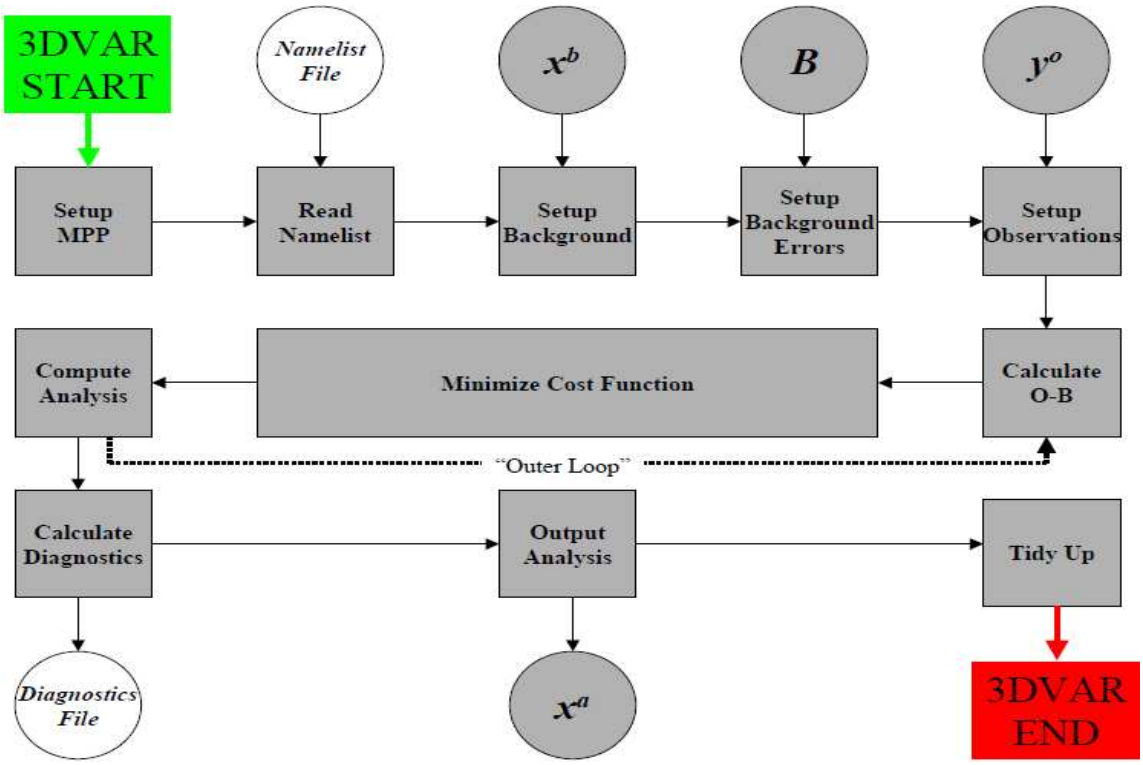

FIG. 5. Inner details of 3DVAR after Barker et al. (2004).

3.3. Experimental Designs

A total of eight high-resolution WRF experiments were performed to evaluate different combinations of observation nudging, grid nudging, and 3DVAR during the high-impact AR event (Table 1). The control experiment (CTRL) has no data assimilation. The experiments that include FDDA nudging methods used Cressman-style objective analysis from the OBSGRID program in order to improve the initial and boundary conditions throughout the model integration at 3-h intervals. Depending on the experiment, either just the HMT surface station data or both the HMT surface and NWS sounding data were assimilated. Figure 6 shows the locations of all HMT surface stations and NWS soundings used in this study.

In the second experiment, SN1, observation nudging was used solely with the HMT surface sites. Only the HMT surface data were used in SN1 to study how effective surface observation nudging is on the QPFs. Observation nudging was performed at 3-h time intervals throughout the entire forecast period. Although observation nudging is best for real-time and almost-continuous data assimilation, a relatively coarse 3-h nudging time interval was chosen for all other experiments that use a FDDA nudging method because of computer power restraints in assimilating over the 138-h forecast. All stations were assigned a RIN_{xy} of 40 km with observation nudging coefficients of 3.0 x 10^{-4} s^{-1} for temperature, moisture, and horizontal winds.

Experiments N2 and N3 combined both observation nudging and grid nudging, and they included both HMT surface data and upper-level NWS sounding data. Grid nudging was included both at the surface and in the upper levels. N2's RIN_{xy} was

increased to 100 km for all surface and upper air observations. Pattantyus (2011) suggested that a larger RIN_{xy} for mesoscale FDDA observation nudging in WRF produces more realistic precipitation patterns in comparison to radar returns in short-range forecasts. N2 has the same observation nudging coefficients as SN1 but with grid nudging coefficients of 6.0×10^{-4} s^{-1}. In order to test the effects of different RIN_{xy} values for the upper air soundings and surface data, an upper air RIN_{xy} of 120 km and a surface RIN_{xy} of 60 km were chosen. Both N2 and N3 also have nudging intervals of 3 h.

TABLE 1. WRF Experimental Designs.

Experiment	**Starting Model**	**DA Method(s)**	**Data Used**	**DA Specifics**
CTRL	GFS 0.5°	none	--------	--------
SN1	GFS 0.5°	observation nudging	HMT surface	RIN_{xy} = 40 km $G = 6.0 \times 10^{-4}$ s^{-1} time interval = 3 h
N2	GFS 0.5°	observation & grid nudging	HMT surface + RAOB	RIN_{xy} = 100 km $G = 6.0 \times 10^{-4}$ s^{-1} time interval = 3 h
N3	GFS 0.5°	observation & grid nudging	same as N2	Same as N2 except: surface RIN_{xy} = 120 km upper air RIN_{xy} = 60 km
3DVT1	GFS 0.5°	3DVAR cold-start + observation & grid nudging	HMT surface + RAOB + COSMIC GPS RO	3DVAR: t_0 window = 12 h Nudging: same as N3
3DVT2	GFS 0.5°	3DVAR cold-start	same as 3DVT1	t_0 window =12 h
3DVT3	GFS 0.5°	3DVAR cycl.	same as 3DVT1	cycling window = 3 h
3DVT3 ERA	ERA-Interim	3DVAR cycl.	Same as 3DVT1	cycling window = 3 h

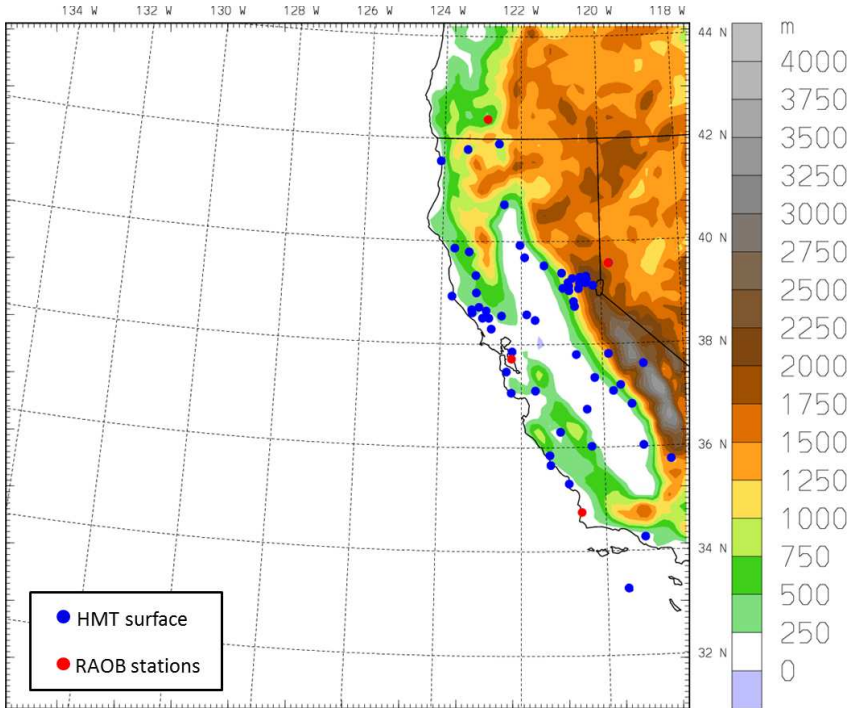

FIG. 6. Locations of HMT surface stations (blue dots) and NWS radiosonde observations (RAOB) (red dots) within D1.

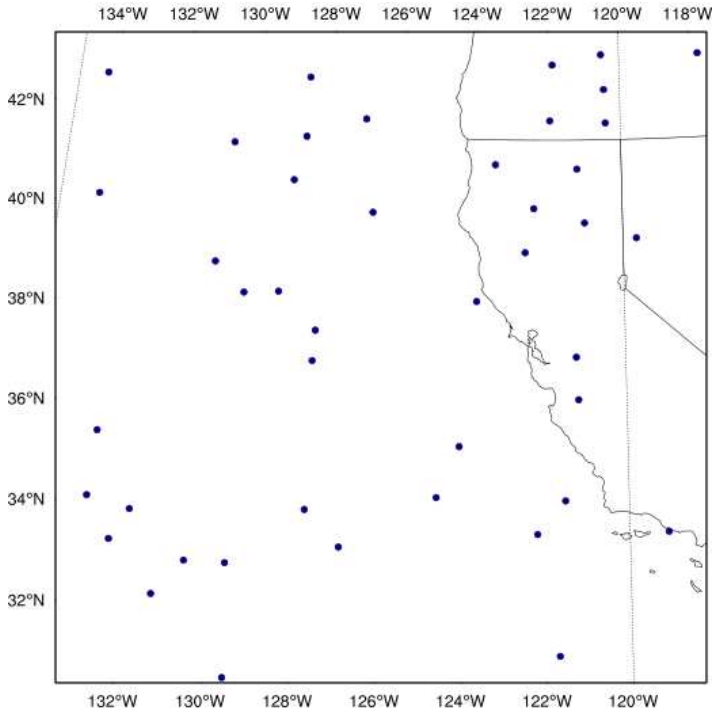

FIG. 7. Locations of all 46 COSMIC GPS RO soundings within D1 from 0000 UTC 28 November to 1800 UTC 03 December 2012.

The last four experiments included COSMIC GPS RO data and the 3DVAR method but with different data assimilation combinations. Only 46 COSMIC GPS RO soundings were available throughout the event and within the parent domain. The scattered spatial distribution of the RO soundings is shown in Figure 7. The 3DVT1 experiment is a hybrid of all three data assimilation techniques (observation nudging, grid nudging, and 3DVAR), and it included all data sources (HMT surface, upper air soundings, and COSMIC data). Also, it has the same settings as N3, but it performed cold-start 3DVAR at the model starting time with a relatively large 12-h time window to take advantage of as many COSMIC GPS RO profiles as possible. 3DVT2 is purely a cold-start 3DVAR run with the same 12-h time window as 3DVT1 but without nudging. 3DVT3 is a 3DVAR cycling run with both a cycling interval and observation time window of 3 h. Not every 3-h window had COSMIC soundings available, and there was only an average of one sounding within the parent domain per 3-h time window (Fig. 8). 3DVT3 ERA is the 3DVT3 experiment but with ERA-Interim data for initial and boundary conditions instead of GFS 0.5 degree. The purpose of 3DVT3 ERA was to test how 3DVAR cycling performs with different initial conditions.

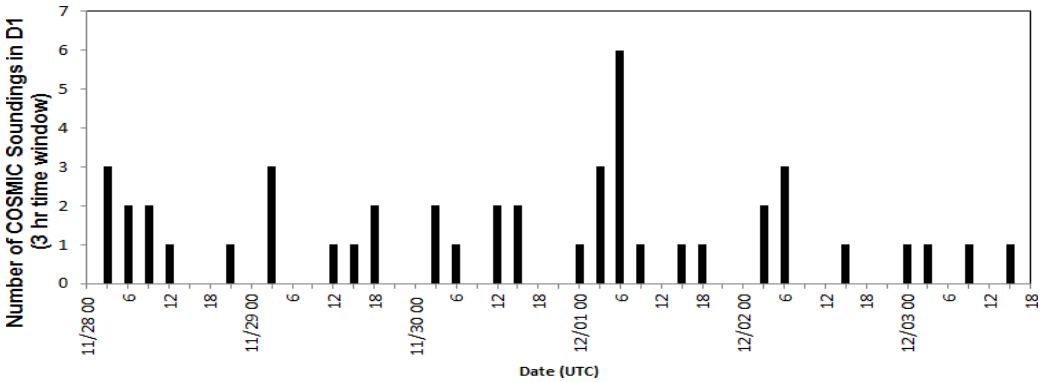

FIG. 8. Number of COSMIC Soundings in D1 per 3-h time window.

4. Synoptic and Mesoscale Overview

From 0000 UTC 28 November to 1800 UTC 03 December 2012, four AR episodes made landfall over northern and central California. A deep longwave trough was present over the northeastern Pacific Ocean upstream of an amplified ridge from the Pacific Northwest to Alaska. This blocking event persisted and allowed the upper air pattern to become quasi-stationary. Multiple shortwave troughs circulated around the longwave trough and brought four AR episodes of high IWV content and heavy precipitation to California within six days (Fig. 9a-d). The NWS issued multiple flash flood and high wind warnings across many northern California counties (NCDC 2012). All episodes except Episode 3 showed stronger, more well-defined landfalling ARs with IWV values greater than or equal to 30 mm and maximum IWV values possibly exceeding 40 mm. Values of NARR vertically integrated horizontal water vapor transport (IVT) from the surface to 300 hPa (Neiman et al. 2008) exceeded 800 kg $m^{-1}s^{-1}$ with Episode 4 showing very strong values greater than 1000 kg $m^{-1}s^{-1}$ (Fig. 10). Heavy rainfall within the frontal bands prevented SSMIS from getting IWV retrievals in the ARs' cores. Although the moisture source during Episode 1 originated more directly from the tropics, it was not as wide and not as perpendicular to the coast as Episodes 2 and 4.

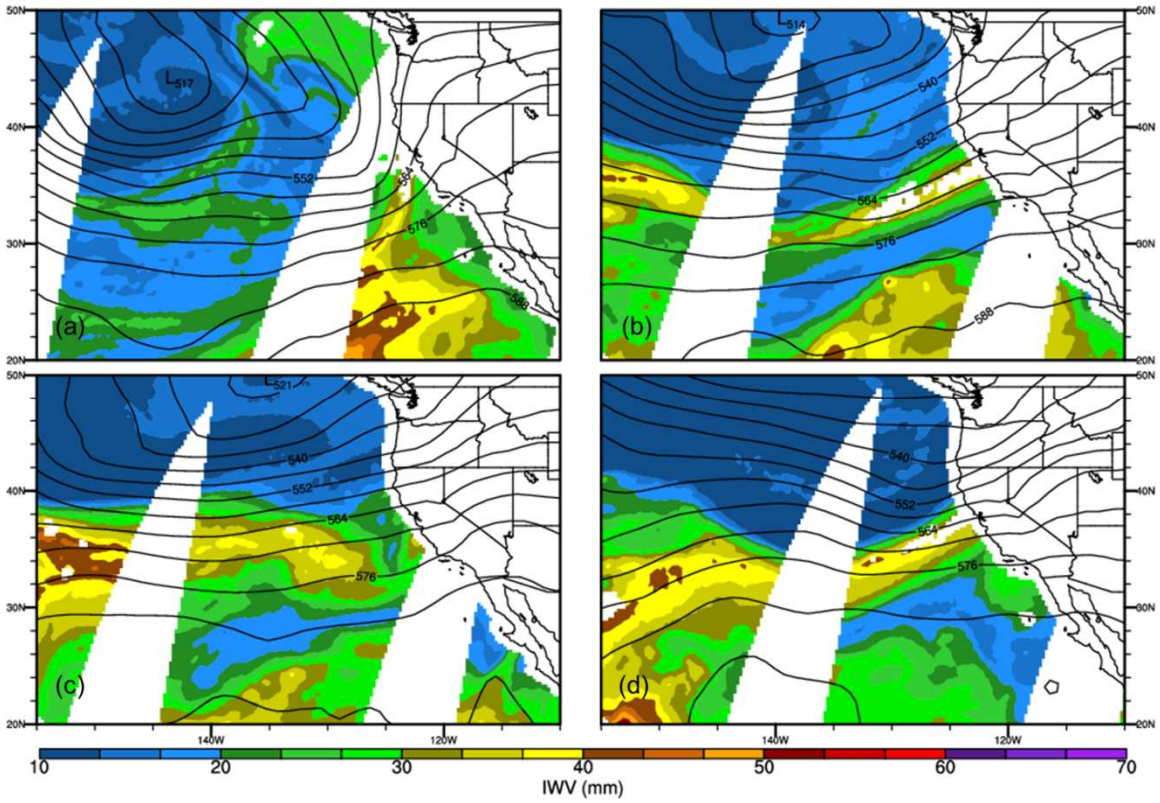

FIG 9. SSMIS IWV for AR Episodes 1-4 (a-d) overlaid with the most recent 500-hPa NARR height analysis (dam): (a) Episode 1 (28 Nov): 1518 UTC SSMIS / 1500 UTC NARR; (b) Episode 2 (30 Nov): 1623 UTC SSMIS/ 1500 UTC NARR; (c) Episode 3 (01 Dec): 1441 UTC SSMIS / 1500 UTC NARR; and (d) Episode 4 (02 Dec): 1600 UTC SSMIS/ 1500 UTC.

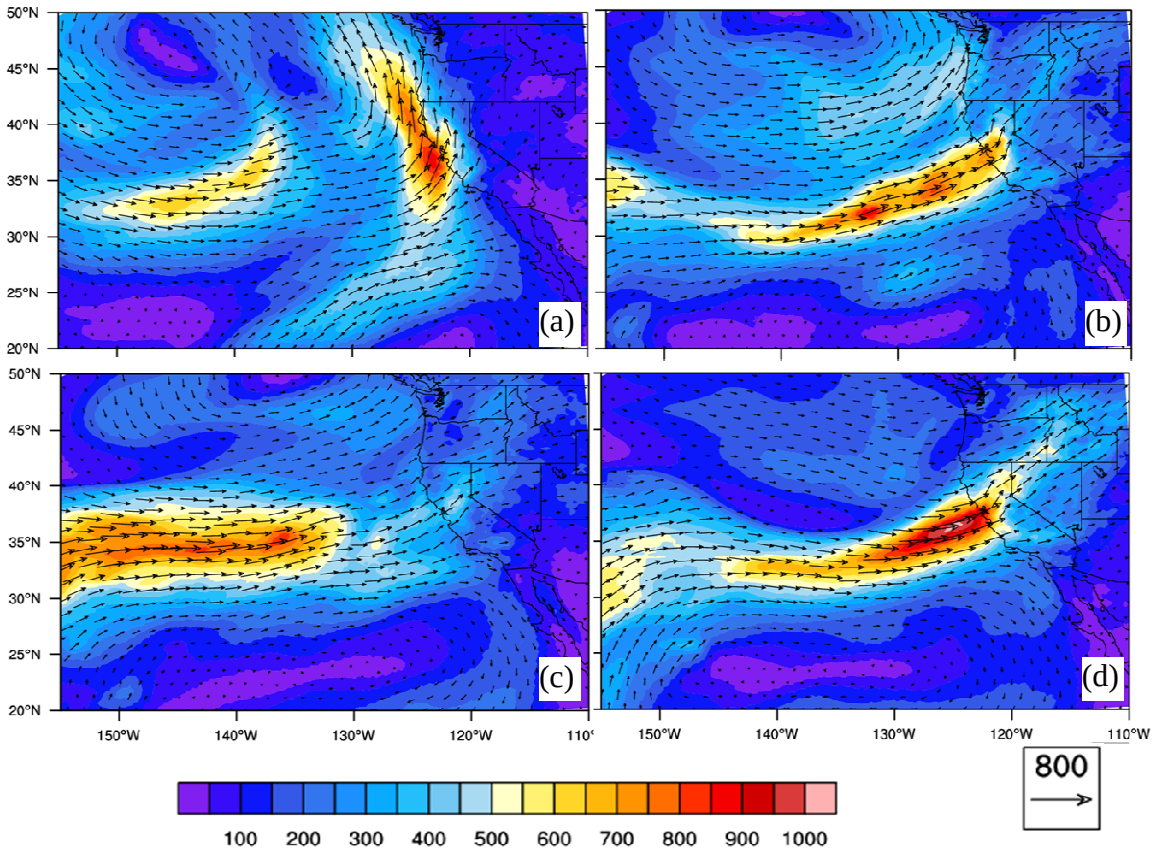

FIG. 10. Vertically integrated horizontal water vapor transport (IVT; kg s^{-1} m^{-1}) derived from NARR for all 4 AR episodes: (a) Episode 1 (1500 UTC 28 Nov); (b) Episode 2 (1200 UTC 30 Nov); (c) Episode 3 (1500 UTC 01 Dec); (d) Episode 4 (1500 UTC 02 Dec). The direction and magnitude of IVT is displayed with the black vectors. The reference IVT vector is 800 kg s^{-1} m^{-1}).

TABLE 2. Maximum 6- and 12-h rainfall rates for each AR episode.

Episode	**Landfall Time Period**	**Largest NCEP Stg. IV 6-h Rainfall Rates**		**Largest NCEP Stg IV 12-h Rainfall Rates**	
		Ending Time	**6-h Rate** mm $(6\ h)^{-1}$	**Ending Time**	**12-h Rate** mm $(12\ h)^{-1}$
1	1200 UTC 28th - 0000 UTC 29th	1800 UTC 28th	62	0000 UTC 29th	77
2	1200 UTC 29th - 0600 UTC 1st	1800 UTC 30th	131	0000 UTC 1st	195
3	1200 UTC 1st - 0000 UTC 2nd	1800 UTC 1st	104	0000 UTC 2nd	114
4	0000 UTC 2nd - 0600 UTC 3rd	1200 UTC 2nd	110	1800 UTC 2nd	190

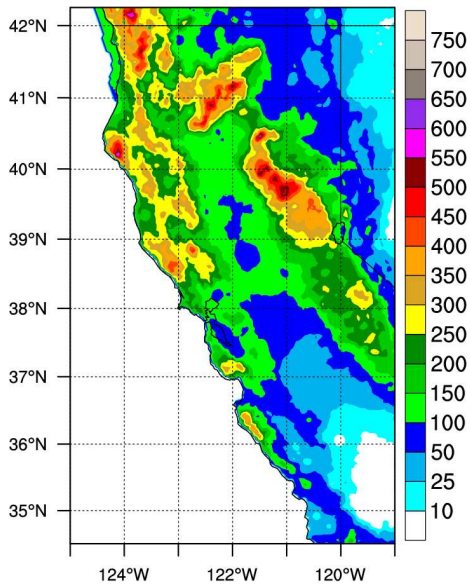

FIG. 11. NCEP Stg. IV accumulated rainfall (mm) for entire event from 0000 UTC 28 November to 1800 UTC 03 December.

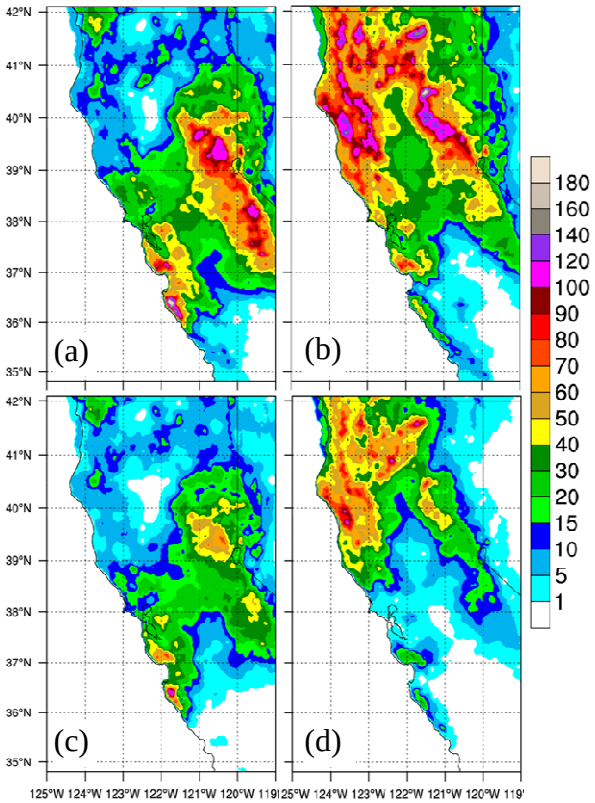

FIG. 12. NCEP Stg. IV time periods with the maximum 12-h (a-b) and 6-h (c-d) rainfall accumulations (mm) for Episode 2 (a,c) and Episode 4 (b,d) from Table 2.

This event brought strong orographic precipitation to most of Northern California. Figure 11 shows the entire event rainfall accumulations from NCEP Stage IV rainfall analysis. The three regions that experienced the highest orographic rainfall totals were the Coastal Range, northern Sierra Nevada/extreme southern Cascades, and the Trinity Alps/Mount Shasta region. The event maximum of 588 mm (~23.15 in) occurred in Humboldt County, located in the northern Coastal Range. In order to identify when and where the heaviest rainfall rates occurred, every 6- and 12-h interval in the NCEP stage IV data were studied to find the time period and episode that received the highest 6- and 12-h accumulations, respectively. Table 2 shows the largest 6- and 12-h accumulations for all four episodes along with their time periods. Both Episodes 2 and 4 had the largest 6- and 12-h accumulations overall with Episode 2 showing slightly higher 6-h and 12-h rainfall rates of 131 mm (1200—1800 UTC 30th) and 195 mm (1200 UTC 30th—0000 UTC 1st), respectively, along the windward slopes of the Santa Lucia Mountain Range (Fig. 12), which has one of the steepest coastal reliefs in the continental United States (Hapke 2005). Although Episode 4 caused more widespread heavy rainfall across most of Northern California, it did not produce the largest localized maximum 6-h and 12-h rainfall rates. The NWS sounding from Oakland (KOAK) during Episode 2 at 1200 UTC shows a strong LLJ moving onshore with southwest winds of 50-55 kt (~26-28 m s^{-1}) between 850 and 900 hPa and with nearly saturated conditions (Fig. 13). Therefore, the evaluation of the WRF experiments mostly focused on Episode 2's period of highest 6-h orographic rainfall rate in D2 (i.e., forecast hours 60-66).

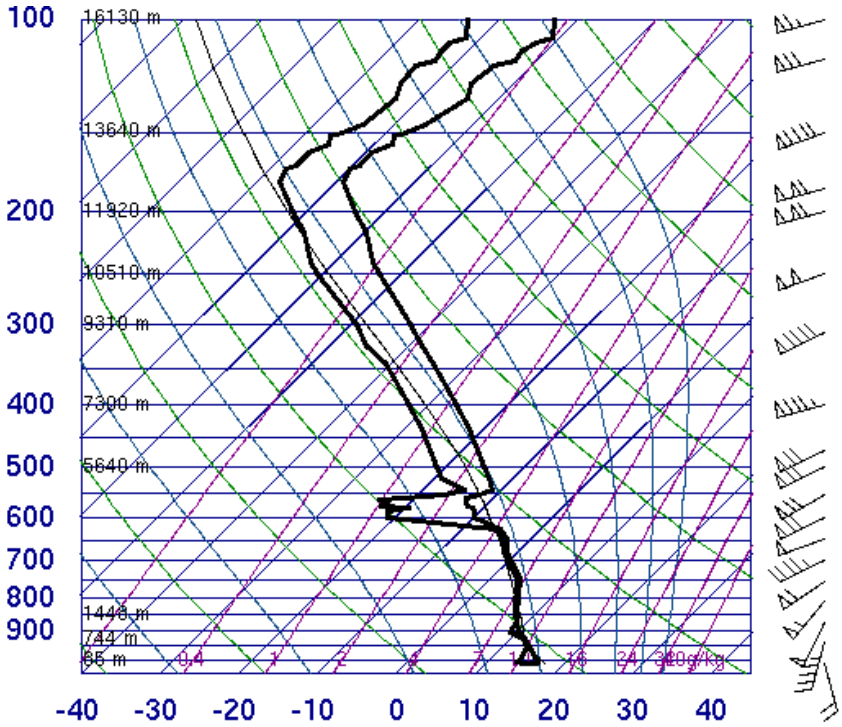

FIG. 13. Skew-t sounding from Oakland, CA (KOAK) valid at 1200 UTC 30 November 2012. Wind barbs on the right depict wind speed (knots). (Image from http://weather.uwyo.edu/upperair/sounding.html)

5. Experiment Results

5.1. Characteristics of AR Episode 2

To evaluate the performance of the WRF experiments during Episode 2's maximum 6-h rainfall time period (1200 to 1800 UTC 30 November), the experiment results of accumulated rainfall during this 6-h period were compared to NCEP Stage IV rainfall estimates (Fig. 14). All WRF experiments did not capture the correct location and timing of the front associated with the AR 66 h into the forecast (Figs. 14b-i). The experiments were much slower to progress the cold front associated with the AR southward. In addition to the timing error, the simulations were not able to correctly predict the localized rainfall maximum in the coastal windward slopes of the Santa Lucia Mountains. They underestimated the rainfall by about 60-70 mm in the next 6-h period (not shown). 3DVT3 ERA (Fig. 14i) shows the most realistic results in this time period by producing 20-30 mm of rainfall further south along the windward slopes of the Santa Lucia Range, a slightly more southward front, and less rainfall behind the front.

Also, all WRF experiments with GFS initial conditions [hereto referred as WRF-GFS experiments (Figs. 14b-h)] overestimated the rainfall behind the front in the northern Coastal Range, Trinity Alps, and Mount Shasta regions. In addition, a large wet bias exists in the Sacramento Valley for all experiments. With respect to frontal position, all experiments with grid-nudging (N2, N3, and 3DVT1) depict a more N-S orientation of the front in the Sacramento Valley, whereas the ones without grid nudging (CTRL, SN1, 3DVT2, 3DVT3, and 3DVT3 ERA) show a frontal angle that matches more closely to NCEP stage IV.

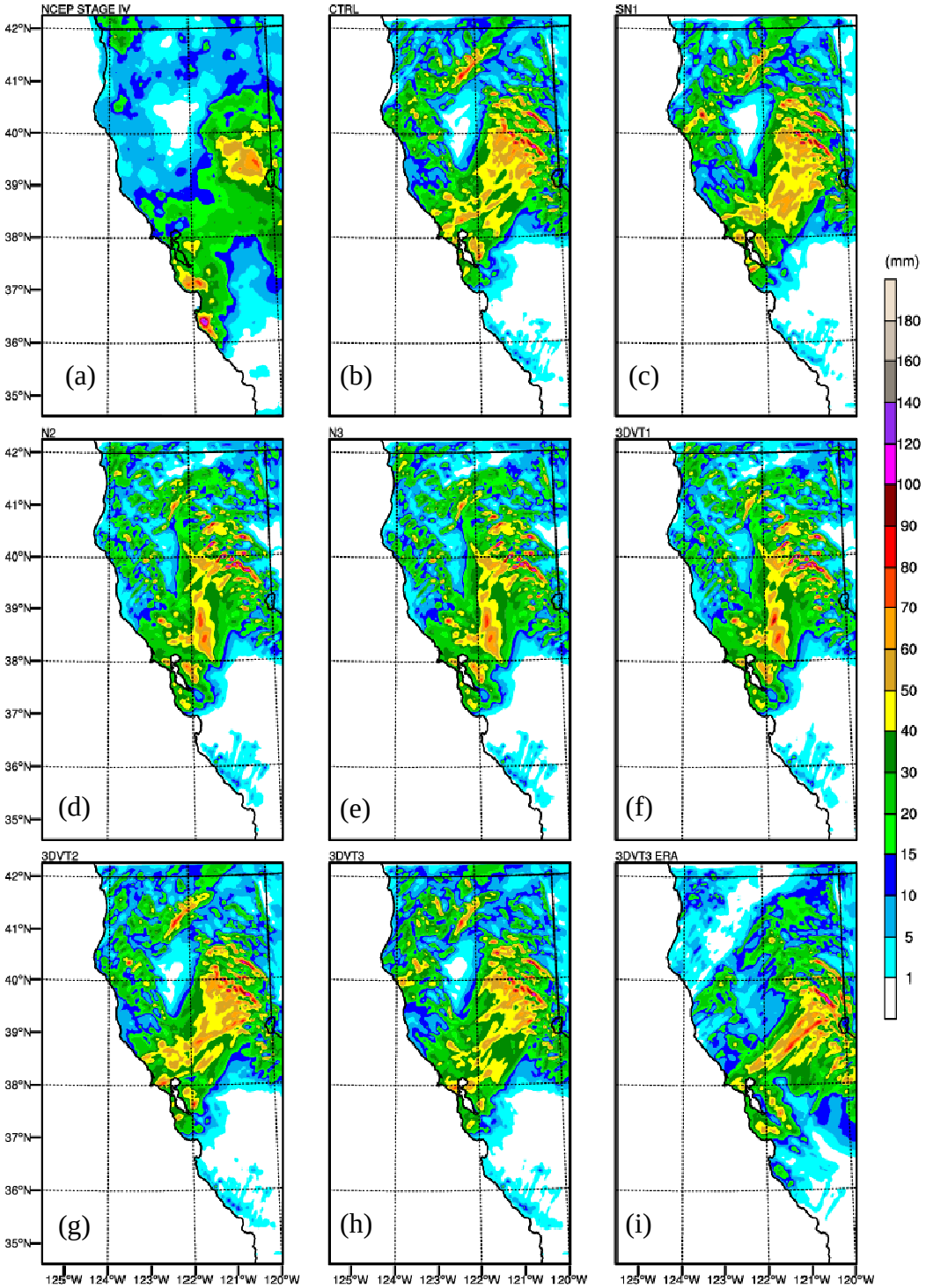

FIG. 14. 6-h accumulated rainfall during AR Episode 2 ending at 1800 UTC 30 November in D2 for (a) NCEP Stg. IV (b) CTRL (c) SN1 (d) N2 (e) N3 (f) 3DVT1 (g) 3DVT2 (h) 3DVT3 (i) 3DVT3 ERA.

In addition to the accumulated precipitation during Episode 2, the experiments' representations of the AR in terms of IWV values were compared to SSMIS observations (Fig. 15). At 1623 UTC, SSMIS IWV observations (Fig. 15a) show an AR with core IWV values of 37-40 mm and with its central axis just south of Monterey Bay. Nevertheless, the WRF experiments at 1600 UTC (Figs. 15b-i) show the AR lagging by a few hours with their central axes at the San Francisco Peninsula and with less-perpendicular orientations than observations. Although SSMIS could not get measurements near the coast, inland, or in the heavy rainfall, it can be inferred from Figure 15a that there were higher IWV values closer to the coast than the WRF experiments.

Only subtle differences in the landfalling AR exist between the WRF-GFS experiments (Figs. 15b-h). The WRF-GFS models that applied grid nudging show weaker IWV values but had a larger AR width (Figs. 15d-f), and the ones without grid nudging show a thinner core AR but with more accurate maximum IWV values (Figs. 15b-c, g-h). Of the WRF-GFS experiments, SN1 shows the best improvement by showing a farther extension of higher IWV values closer to the San Francisco Peninsula.

3DVT3 ERA's AR horizontal structure (Fig. 15i) matched closest to SSMIS observations because it extended higher values of IWV (33-37 mm) closer to the coast with a broader core and it showed higher IWV values farther south along the coast. Like SSMIS observations, 3DVT3 ERA did not show IWV values greater than 20 mm north of 39 °N. Weaker IWV values closer to the coast and a less perpendicular AR angle are two possible explanations for why the WRF experiments could not accurately predict the

maximum rainfall amount in the Santa Lucia Mountains during Episode 2.

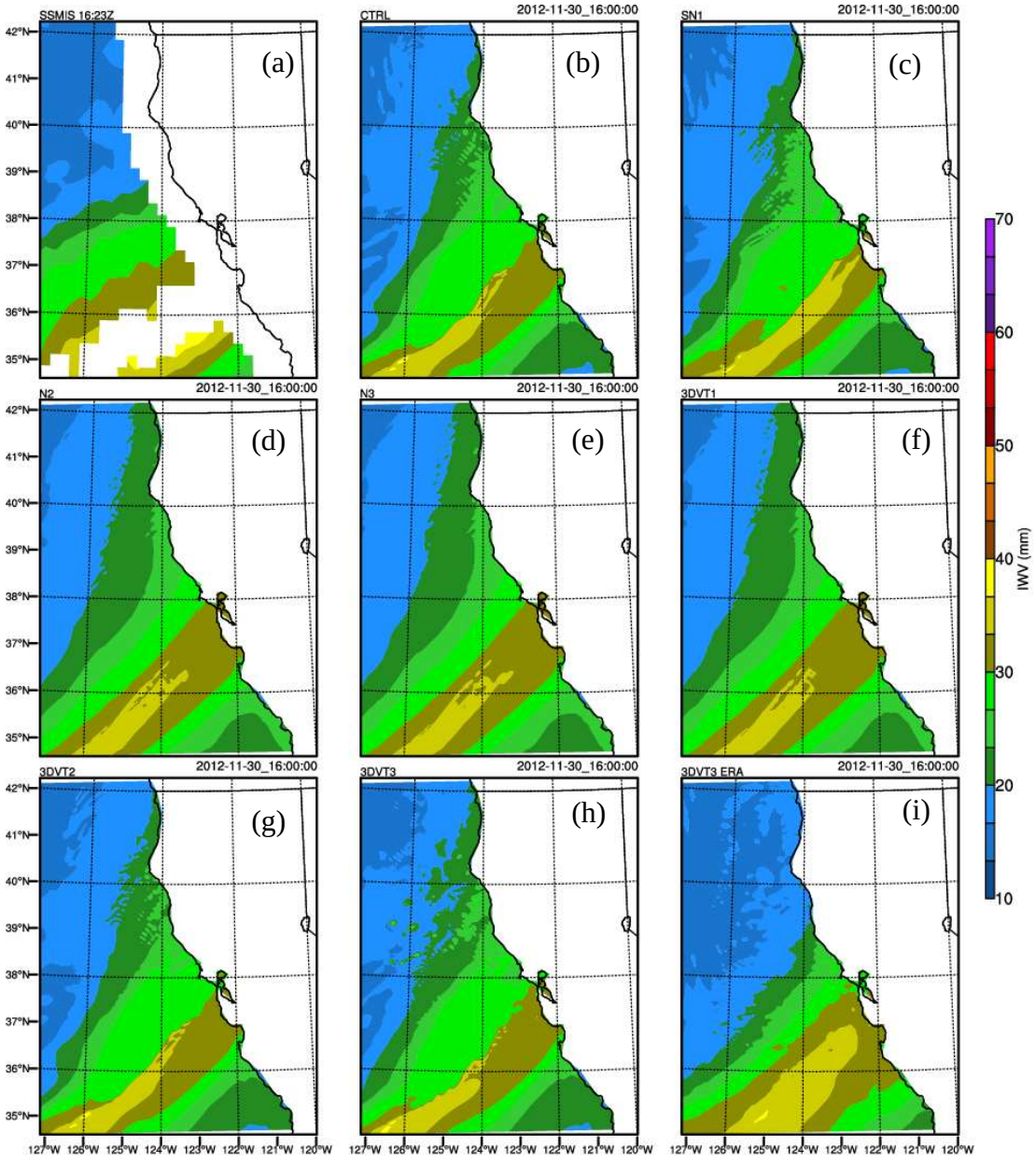

FIG 15. IWV in D2 during AR Episode 2 on 30 November 2012 for (a) SSMIS at 1623 UTC and the WRF experiments (b-d) valid for 1600 UTC: (b) CTRL (c) SN1 (d) N2 (e) N3 (f) 3DVT1 (g) 3DVT2 (h) 3DVT3 (i) 3DVT3 ERA.

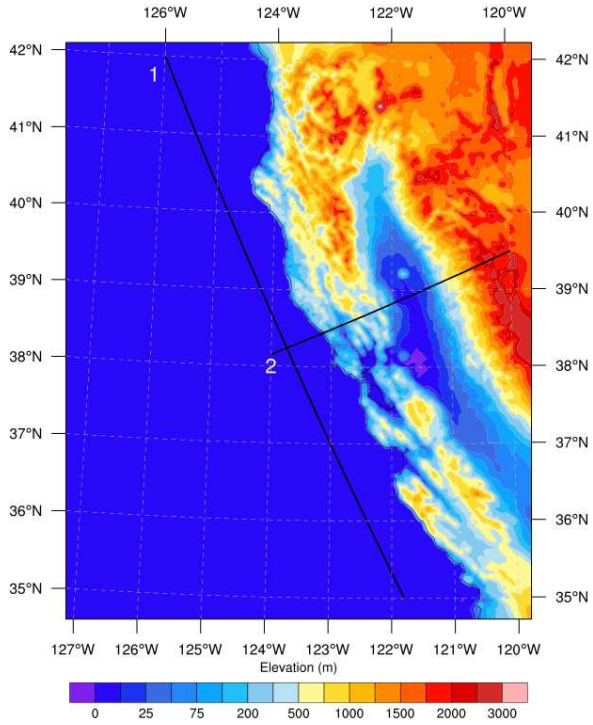

FIG. 16. N-S along-coast cross section (Line 1) and W-E cross section through the Sacramento Valley (Line 2).

Analysis into the onshore and inland moisture flow, dynamics, and timing of the AR within Episode 2 was performed in the vertical dimension. A N-S cross section along the California coast and a W-E cross section across the Sacramento Valley were constructed within D2 (Fig. 16). Both cross sections were taken in the middle of the 6-h time period at forecast hour 63 (1500 UTC 30 November). Figure 17 shows the N-S cross section (Line 1 in Fig. 16) of relative humidity and wind speed for the experiments. They all show a frontal inversion, an upper-level jet of 55-60 m s^{-1} and a LLJ on the warm side of the front greater than or equal to 20 m s^{-1} near 1 km. The model's representation of these features is consistent with dropsonde observations of landfalling LLJs in ARs (Ralph et al. 2004). The grid-nudging experiments show slightly weaker

low-level winds between 3 and 4 km ahead of and behind the main cold front. Also, they do not show convective updrafts behind the front, whereas the non-grid-nudging experiments do.

The most notable difference between the WRF-GFS experiments (Figs. 17a-g) is the substantial smoothing of the results in the grid-nudging experiments (Figs. 17c-e) versus the finer details in the non-grid-nudging experiments (Figs. 17a-b, f-g). These results are most likely caused by nudging the finer scale model grid-points in D2 toward the coarser objective analysis grids. Stauffer and Seaman (1994) suggested that assimilating relatively coarse-resolution gridded data onto a finer-scale grid does more harm than good by preventing the model's innate ability to develop finer-scale details.

3DVT3 ERA (Fig. 17h) shows slightly better timing of the front but with a more relaxed frontal inversion and a shallower layer of moisture behind the cold front. 3DVT3 ERA also shows LLJ wind speeds of 25-30 m s^{-1} at 1.5 km, and they are closer to the wind speeds observed on the Oakland sounding. The slightly better timing and more accurate LLJ wind speeds seen here is the effect of using reanalysis data as initial and boundary conditions.

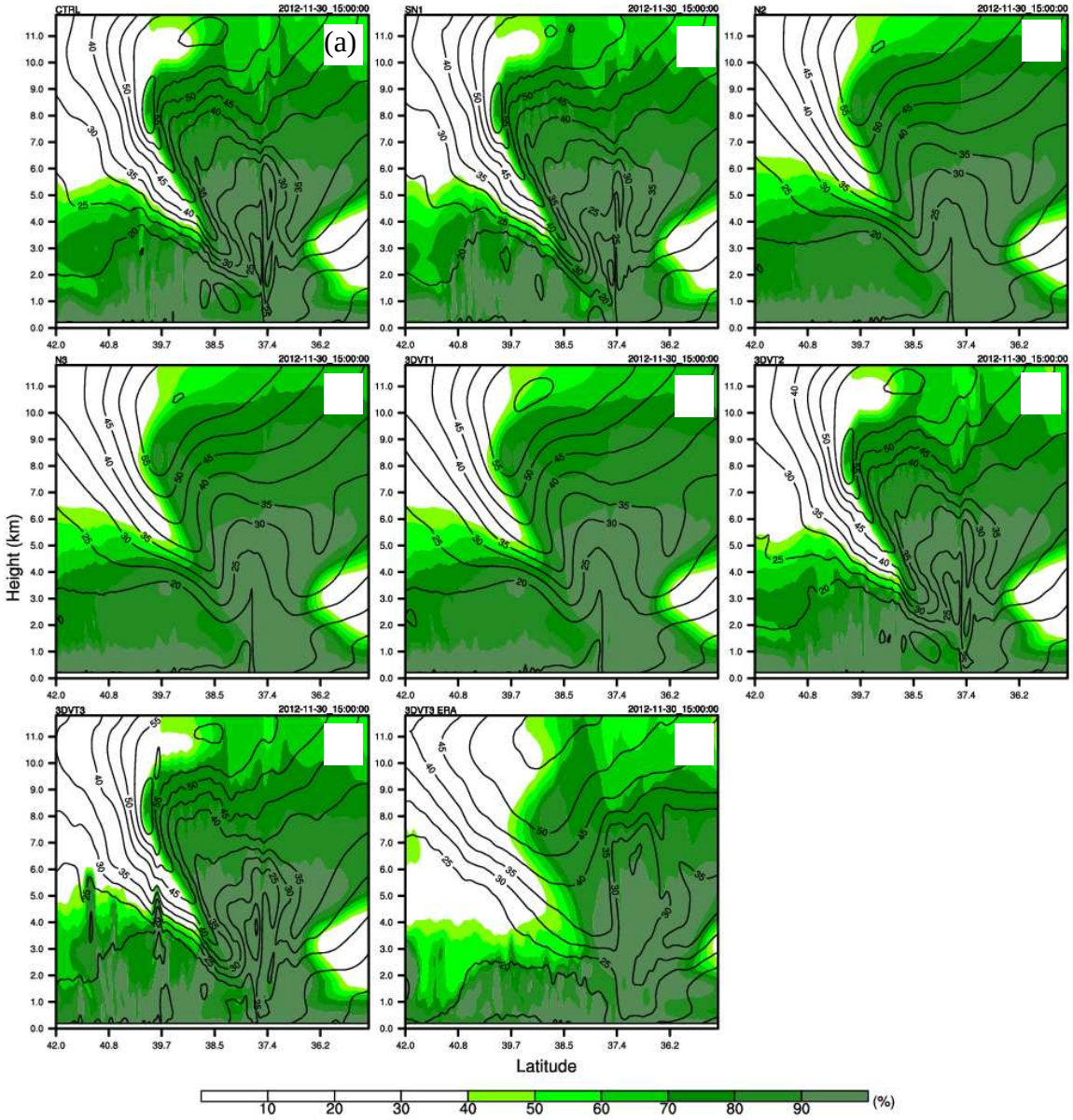

FIG. 17. N-S along-coast vertical cross section (Line 1) of relative humidity (shaded contours) and wind speed (m s^{-1}) (solid black contour lines) during AR Episode 2 at forecast hour 63 (1500 UTC 30 November) for each experiment: (a) CTRL (b) SN1 (c) N2 (d) N3 (e) 3DVT1 (f) 3DVT2 (g) 3DVT3 (h) 3DVT3 ERA. Wind speed contour interval is 5 m s^{-1}.

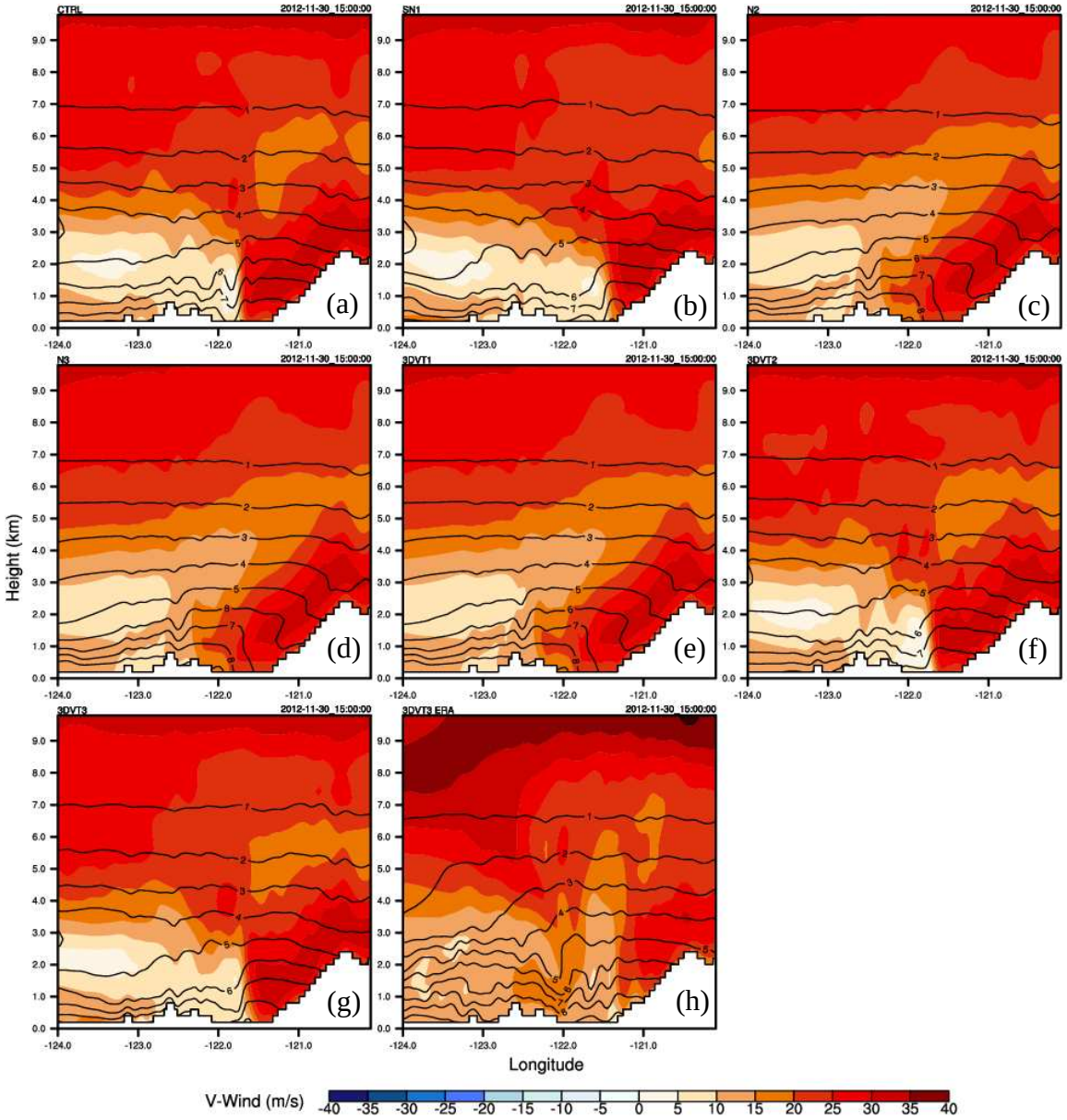

FIG. 18. W-E cross section across Sacramento Valley (Line 2) of the v-wind component (m s^{-1}) (shaded) and specific humidity (g kg^{-1}) (solid black contours) during Episode 2 at forecast hour 63 (1500 UTC 30 November) for each experiment: (a) CTRL (b) SN1 (c) N2 (d) N3 (e) 3DVT1 (f) 3DVT2 (g) 3DVT3 (h) 3DVT3 ERA. The specific humidity contour interval is 1 g kg^{-1}.

Differences in the frontal positions between all experiments can be seen more clearly in the W-E vertical cross section of specific humidity and the meridional wind, or v-wind, component (Fig. 18) in the Sacramento Valley. In Episode 2, the grid-nudging models (Figs. 18c-e) were slower to bring the front across the valley than all the non-grid-nudging models (Figs. 18a-b, f-h) and still had the cold front moving through the Coastal Range. Of the WRF-GFS non-grid-nudging models (Figs. 18a-b, f-g), SN1 was the most progressive and most accurate in its movement and timing of the front. SN1 and 3DVT3 show more evidence that a post-frontal coastal barrier jet formed with higher near-surface southerly wind speeds in the Pacific Ocean west of the Coastal Range. Also, all the non-grid-nudging experiments show a stronger connection between the upper-level winds and the surface cold front than the grid-nudging experiments. All WRF-GFS experiments show a relatively compressed low-level moisture layer with the non-grid-nudging models showing higher surface values of water vapor mixing ratio off the coast and in the Coastal Range. Again, 3DVT3 ERA has a more advanced position of the front in comparison to all experiments but with a weaker southerly wind component impinging the Sierra Nevada. It also shows a much thicker layer of shallower moisture off the coast than all the WRF-GFS experiments.

In the W-E cross section of the zonal wind, or u-wind, component across the Coastal Range and Sacramento valley (Fig. 19), the non-grid-nudging experiments (Figs. 19a-b,f-h) show stronger winds above the ocean surface between 3 and 4 km reaching down to the surface behind the cold front. Again, SN1 (Fig. 19b) shows the most progressive frontal location in the valley of the WRF-GFS experiments (Figs. 19a-g).

SN1 produces the strongest zonal winds at the surface off all the experiments. The grid-nudging experiments (Figs. 19c-e) do not have the front passing through the Sacramento Valley at this time, and they show a negative u-wind component along with a tongue of drier air sinking down along the windward slopes of the Sierra Nevada. This drier air most likely originated from diabatic cooling of the downdrafts from the orographic precipitation along the windward slopes of the Sierra Nevada. Here, 3DVT3 ERA's surface front is generally in the same location as the other experiments (Fig. 19h).

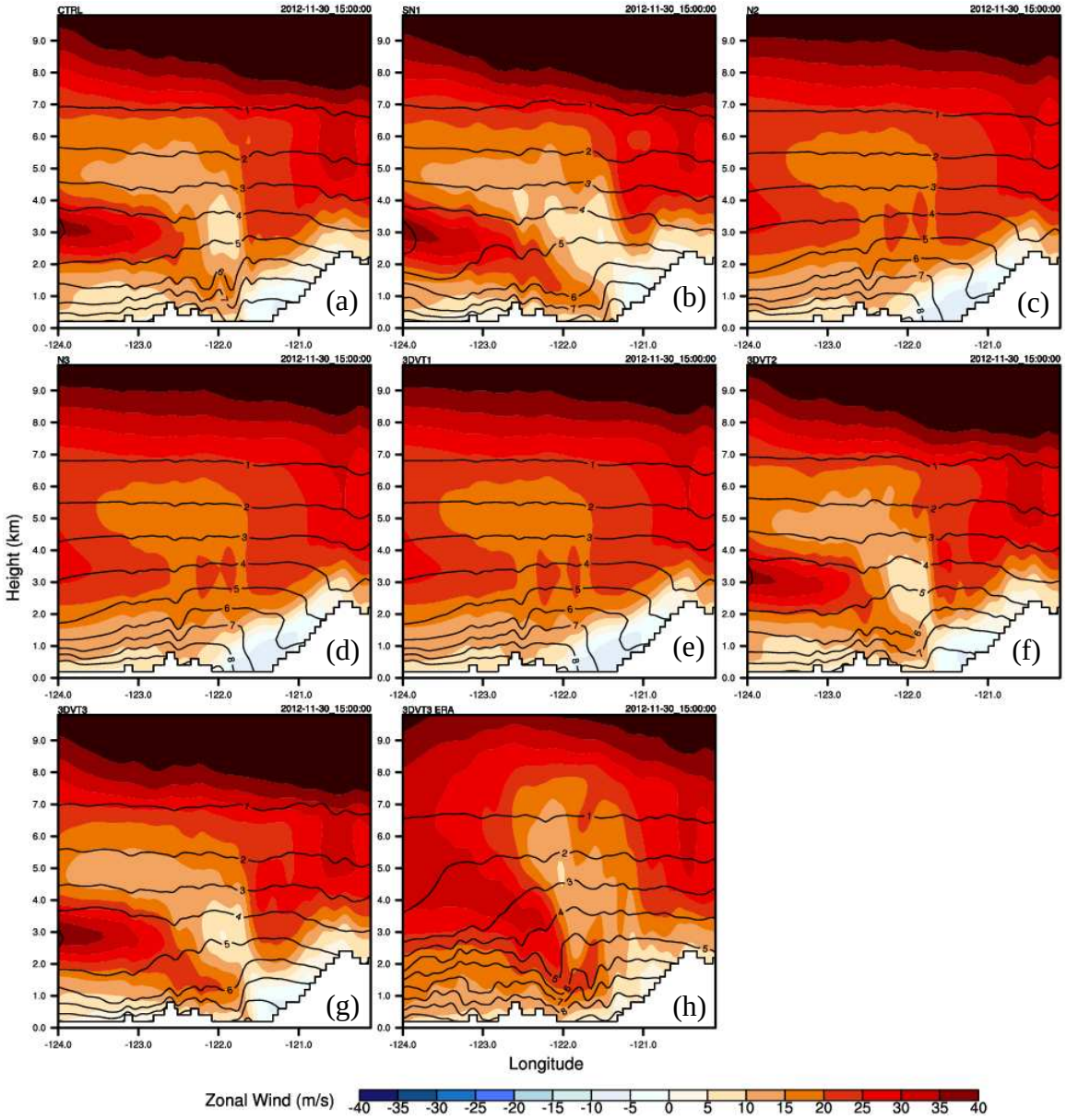

FIG. 19. W-E cross section across Sacramento Valley (Line 2) of the u-wind component (m s^{-1}) (shaded) and specific humidity (g kg^{-1}) (solid contours) during Episode 2 at forecast hour 63 (1500 UTC 30 November) for each experiment: (a) CTRL (b) SN1 (c) N2 (d) N3 (e) 3DVT1 (f) 3DVT2 (g) 3DVT3 (h) 3DVT3 ERA. The specific humidity contour interval is 1 g kg^{-1}.

5.2. Event Total QPFs

To gain a measure of how the simulations performed in terms of QPFs for the entire event (138 h), their total QPF results in D2 were compared to NCEP Stage IV observed total precipitation accumulations (Fig. 20). At the end of the event, all of the models were able capture the general spatial precipitation patterns in most regions, but they resulted in different event accumulation values. The WRF-GFS simulations (Figs. 20b-h) overestimated the precipitation patterns in the higher peaks of the extreme northern Sierra Nevada and extreme southern Cascades northwest of Lake Tahoe, the eastern mountains of the north central Coastal Range, and the higher peaks in the Mount Shasta/Trinity Alps region. Also, they slightly underestimated the rainfall along the northern Coastal Range, especially in the coastal mountains of Humboldt County, which received the highest precipitation accumulations for the entire event, and in the extreme northern coast of California. The grid-nudging experiments (Figs. 20d-f) produced slightly higher precipitation amounts on Mount Shasta, the peaks in the northern Sierra Nevada, and the peaks in the northern Coastal Range than in the non-grid-nudging experiments.

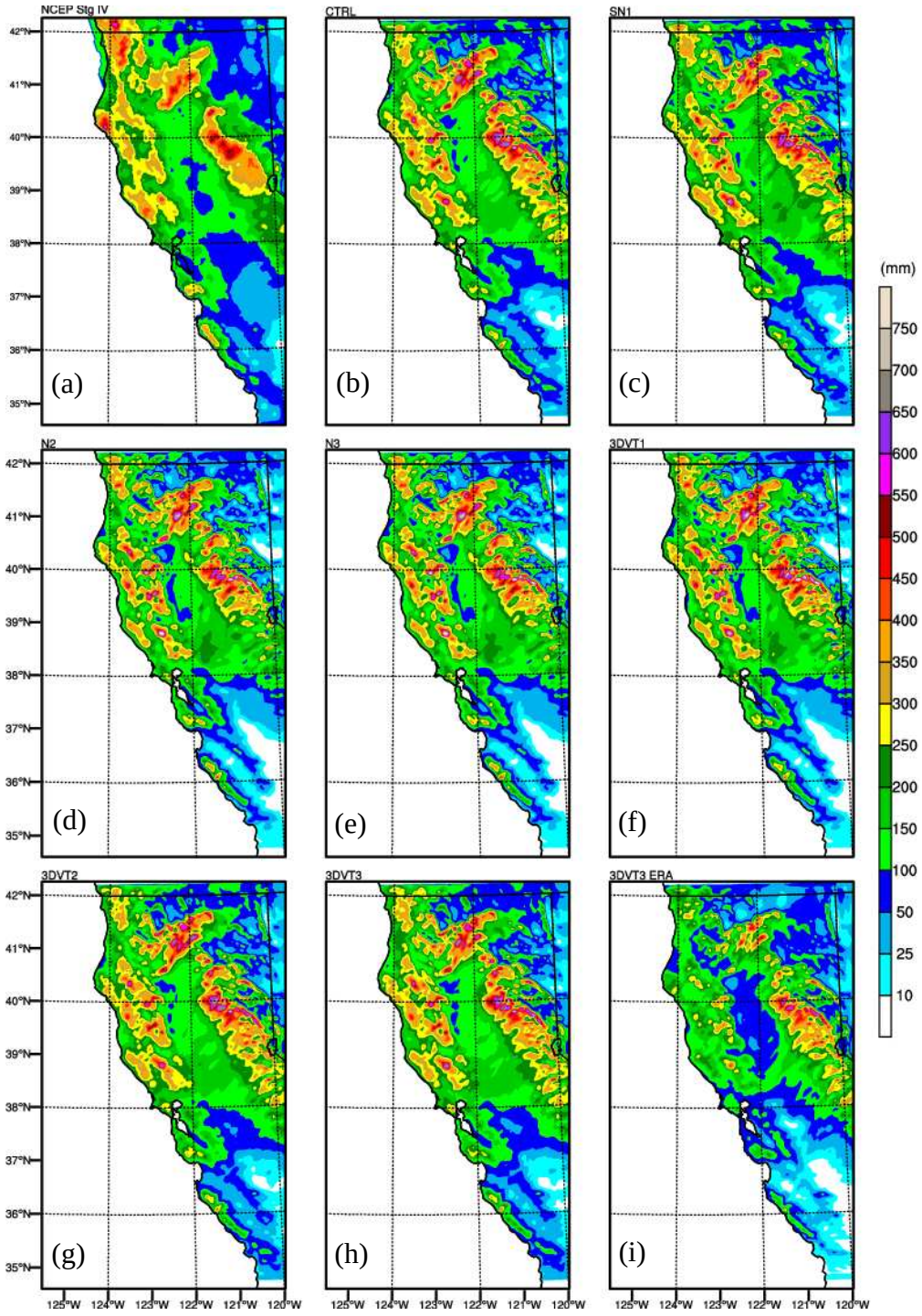

FIG. 20. Accumulated rainfall in D2 for the entire event from 0000 UTC 28 November to 1800 UTC 03 December 2012 for (a) NCEP Stg. IV (b) CTRL (c) SN1 (d) N2 (e) N3 (f) 3DVT1 (g) 3DVT2 (h) 3DVT3 (i) 3DVT3 ERA.

3DVT3 ERA (Fig. 20i) underestimated total precipitation accumulations for most of the Coastal Range, slightly overestimated precipitation in the peaks of the northern Sierra Nevada, and did reasonably well in the Mount Shasta/Trinity Alps region. Although all of the simulations generally overestimated the precipitation in the Central Valley, 3DVT3 ERA produced the most accurate spatial accumulation values there. Using ERA-Interim Reanalysis data, which has a resolution approximately 30 km coarser than GFS 0.5 degree, as initial and boundary conditions was harmful for predicting the coastal orographic precipitation. Even though the WRF experiments used 3 km resolution, it still had the memory of the coarser ERA-Interim data that is not able to accurately resolve the finer terrain features of the Coastal Range.

For a better model intercomparison of event total QPF results and to see the effects of different assimilation methods more completely, difference plots were created for total event accumulations between CTRL and the other experiments (Figs. 21a-g). In general, all nudging experiments (Figs. 21a-d) produced more rainfall in the Sacramento Valley compared to CTRL. More dramatic differences were seen in the grid-nudging experiments (Figs. 21b-d). They produced more precipitation in the Sacramento Valley and in the higher mountains of the Coastal Range but produced less for most of the Sierra Nevada, particularly near Lake Tahoe and further south. There appeared to be no noticeable long-term affect in having different values of RIN_{xy} among the grid nudging experiments. SN1 (Fig. 21a) was the only model to produce more rainfall for most of the entire Central Valley. Also, SN1 produced less precipitation in the Santa Lucia Mountains, whereas the grid-nudging models produced more. Both SN1 and 3DVT3

(Figs. 21a, f) had a very distinct line of contrast in Northern California extending from the Trinity Alps/Mt. Shasta region to the northeast corner of the state with more precipitation on the southeast side of the line of no change and less precipitation on the northwest side. SN1, however, shows a clearer connection between the more precipitation seen in the Sacramento Valley and the area southeast of this contrasting line. The cold-start 3DVAR experiment, 3DVT1 (Fig. 21e), expectedly had the least differences in rainfall from CTRL because only its initial analysis was changed. 3DVT3 ERA (Fig. 21g) dramatically shows much less rainfall than CTRL for most of the entire state except for parts of the northern Sierra Nevada and on their lee side.

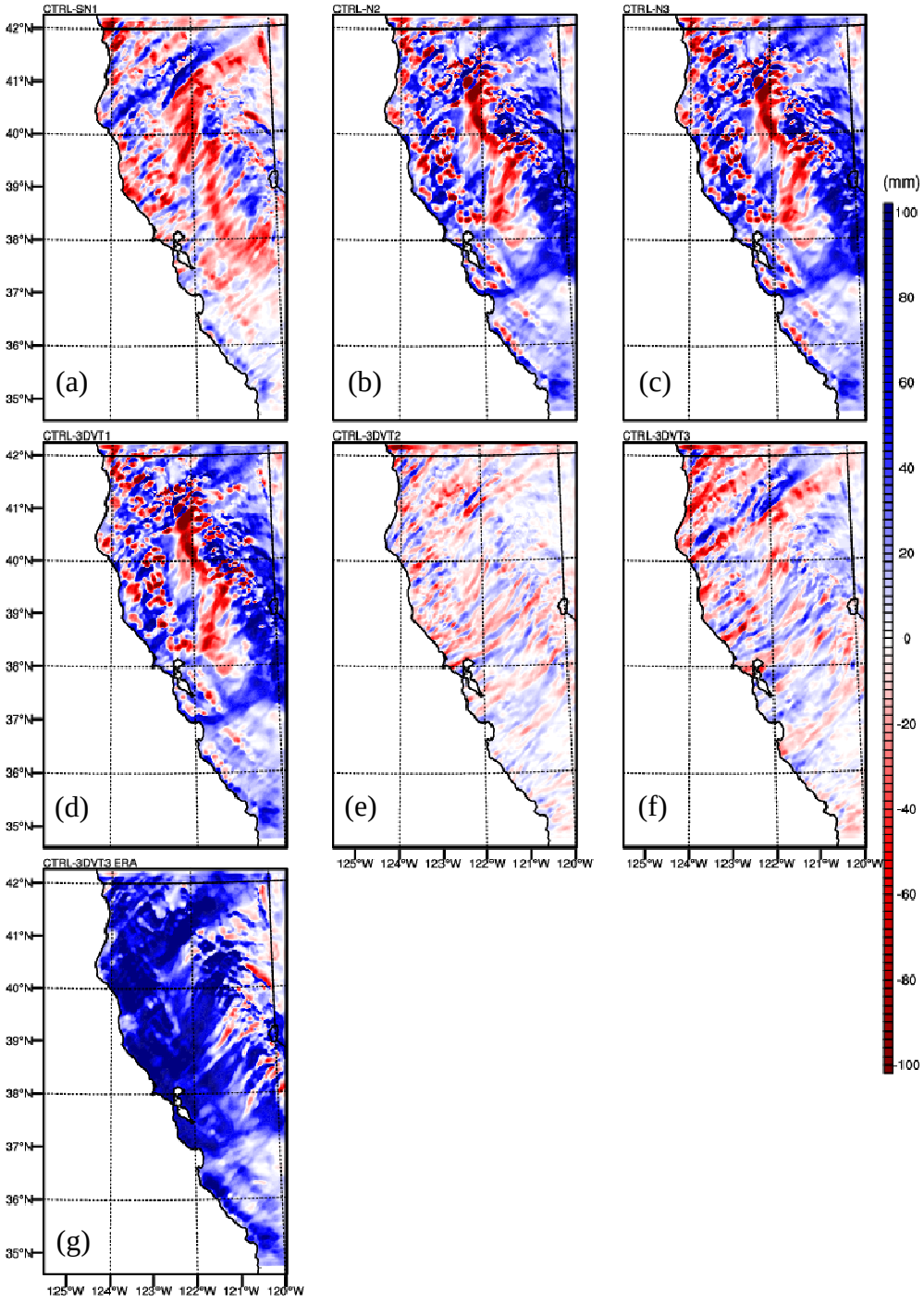

FIG 21. Total event accumulated rainfall difference plots from CTRL experiment for all other experiments (CTRL minus experiment) in D2 for the entire event from 0000 UTC 28 November to 1800 UTC 03 December 2012 for (a) SN1 (b) N2 (c) N3 (d) 3DVT1 (e) 3DVT2 (f) 3DVT3 (g) 3DVT3 ERA.

5.3. Statistical Comparison of Precipitation over Coastal Range and Sierra Nevada

To further evaluate performance in the simulated QPFs among the models, two clusters of HMT surface stations were separated into two regions: the north central Coastal Range and the windward Sierra Nevada (Fig. 22). For each region, all the accumulated rainfall time evolutions for each station were averaged to get a site-averaged accumulated rainfall time series for both the HMT surface observations and the experiments. Locations of the HMT surface sites were interpolated in the WRF experiments in order to get the accumulated rainfall time series. Only HMT stations with consistent rainfall data were used. There were a total of 8 and 13 stations in the north central Coastal Range Region and the windward Sierra Nevada region, respectively.

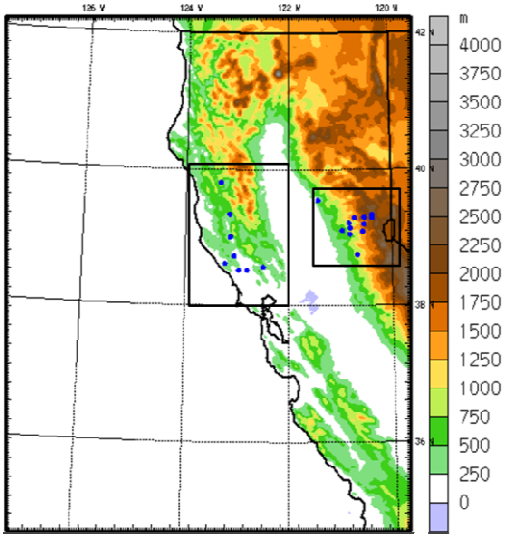

FIG. 22. North central Coastal Range sites (left box) and windward Sierra Nevada sites (right box) for area-averaged HMT sites for entire event accumulated rainfall.

Figure 23 shows the site-averaged accumulated rainfall time evolutions for each of the regions throughout the forecast period. For the north central Coastal Range region (Fig. 23a), all the WRF experiments on average underestimated the rainfall amounts for the first half of the event. Right after Episode 2 and near forecast hour 60, the WRF-GFS non-grid-nudging models (CTRL, SN1, 3DVT2, and 3DVT3) and grid-nudging models (N2, N3, and 3DVT1) diverged in their results. For the rest of the forecast, the WRF-GFS non-grid-nudging models overestimated the rainfall and the grid-nudging models stayed near the observations until the end where they underestimate the rainfall. The WRF-GFS non-grid-nudging models overestimated the rainfall by approximately 15-20 mm, and the grid-nudging models underestimated by about 30 mm. 3DVT3 ERA largely underestimated the rainfall throughout the entire event for this area and on average underestimated the total rainfall by 100 mm at the ending forecast hour. Also, during Episode 2, the other models performed better at simulating the average rainfall rates than 3DVT3 ERA.

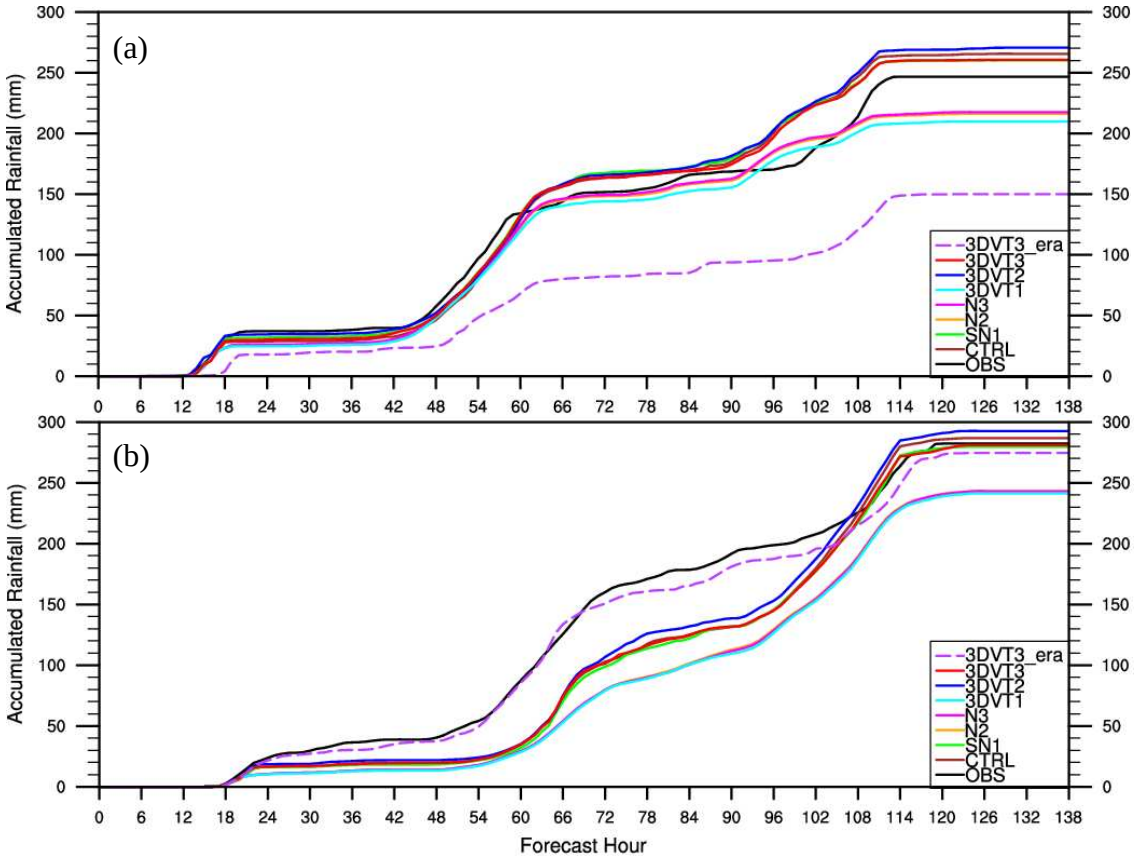

FIG. 23. Area-averaged hourly time series of accumulated rainfall for observations (black line) and all experiments (colored lines) for (a) north central Coastal Range and (b) windward Sierra Nevada.

For the windward Sierra Nevada region (Fig. 23b), 3DVT3 ERA had the most accurate results of the rainfall accumulation time series, staying very close to observations throughout the entire time period. All the other experiments underestimated the rainfall even more than in the north central Coastal Range until Episode 4. Here, the WRF-GFS non-grid-nudging models recovered back to the observations except for the grid-nudging models that showed an underestimation similarly seen in the north central Coastal Range. As seen before in the north central Coastal Range region, the grid-nudging and WRF-GFS non-grid-nudging models in the windward Sierra Nevada also

began to diverge during Episode 2 two-and-a-half days into the forecast. Here, the grid-nudging models underestimated the final result by about 40 mm.

Lastly, the MAE was calculated for each model and for each region with the accumulated rainfall time series (Table 3). The regular error, $|f_i - y_i|$, was also taken at the end of the event, hour 138 (Table 4). For the north central Coastal Range sites, 3DVT3 performed the best with the least MAE of 10.95 mm, and for the windward Sierra Nevada sites, 3DVT3 ERA had the least MAE of only 6.51 mm. In general, the experiments had larger MAE values for the windward Sierra Nevada sites than in the north central Coastal Range, except for 3DVT3 ERA. It had the opposite, showing both the highest MAE for the north central Coastal Range and the least MAE for the windward Sierra Nevada. At the end of the event, SN1 on average best predicted the entire event accumulated rainfall for the north central Coastal Range sites with the least error of 13.58 mm. 3DVT3, on average, best predicted the entire event accumulated rainfall at hour 138 for the windward Sierra Nevada sites with the least error of 1.29 mm.

TABLE 3. Area-averaged MAE of forecasted hourly accumulated rainfall time series.

	MAE (mm)							
	CTRL	**SN1**	**N2**	**N3**	**3DVT1**	**3DVT2**	**3DVT3**	**3DVT3 ERA**
North Central Coastal Range	13.07	11.52	12.12	11.51	14.63	13.44	10.95*	56.16
Windward Sierra Nevada	24.09	24.36	39.89	40.15	41.08	22.72	23.40	6.51*

**least MAE*

TABLE 4. Area-averaged error in forecasted total rainfall at forecast hour 138.

	Error (mm)							
	CTRL	**SN1**	**N2**	**N3**	**3DVT1**	**3DVT2**	**3DVT3**	**3DVT3 ERA**
North Central Coastal Range	18.94	13.58*	30.53	29.07	36.85	23.88	13.90	96.82
Windward Sierra Nevada	4.54	2.58	39.21	39.20	41.04	10.33	1.29*	7.70

**least Error*

6. Summary and Conclusions

Various WRF data assimilation methods of observation nudging, grid nudging, and 3DVAR were evaluated for the high-impact, multi-day AR event for Northern California from 0000 UTC 28 November to 1800 UTC 03 December 2012. The purpose of this study was to determine various ways short-to-medium QPFs could be improved for AR events affecting the U.S. West Coast. This study used combinations of data from the HMT surface stations, NWS network soundings, and COSMIC satellite GPS RO soundings for assimilation. During this event, a total of four ARs impacted California within six days producing heavy orographic rainfall and flash flooding. In particular, the second AR episode produced the highest 6- and 12-h rainfall rates along the windward slopes of the Santa Lucia Mountains along the coast based on NCEP Stage IV rainfall analysis. Therefore, most of the results of the numerical experiments focused on the precipitation forecast during this episode. A total of eight high resolution WRF experiments were designed that employed various WRF data assimilation combinations of observation nudging, grid nudging, and 3DVAR. The last experiment used ERA-Interim Reanalysis data instead of the GFS 0.5 degree forecast data to test 3DVAR with different initial conditions.

Results of the experiments during the period in Episode 2 that had the highest 6-h rainfall rate showed that all WRF experiments were a few hours slower than observations with the timing and location of the AR and its associated cold front 66 h into the forecast. Also, the WRF experiments showed an incorrect landfalling AR angle. The experiments could not recapture the maximum 6-h rainfall rate on the windward slopes of the Santa

Lucia Mountains during Episode 2 and largely underpredicted this amount in future model time steps. Of the WRF-GFS experiments during Episode 2, SN1 showed the best improvement in the timing and location of the front associated with the AR. 3DVAR ERA had the most accurate AR representation in terms of IWV and the 6-h rainfall rate; However, this was most likely because it showed better timing (faster), it had a more accurate angle of the cold front (more south along the coast), and it produced LLJ winds that were closer to observations.

It appears that this under-prediction of rainfall in all the experiments during Episode 2 was associated with the strength and size of the AR and the weaker LLJ winds simulated by the models. Another reason for the under-prediction of rainfall at the coast could be that a fine grid resolution of 3 km may still not be fine enough to resolve cloud microphysics on the steep windward slopes of the Santa Lucia Mountains of the Coastal Range.

Cross sections along the coast and across the Sacramento Valley during Episode 2 revealed that applying grid nudging to the inner domain from a coarser domain may not be ideal for mesoscale precipitation forecasts because it smooths out some mesoscale features which can affect the rainfall forecast amounts. The fact that 3DVT3 ERA showed a stronger and broader LLJ with slightly more low-level moisture during this time in Episode 2 may be a reason why more orographic precipitation was seen here.

Overall, the data assimilation experiments without grid nudging showed the best results in terms of the precipitation forecast time evolution, especially 3DVAR. Even though 3DVT3 ERA showed the best results during Episode 2, it largely underpredicted

the event total amount of orographic rainfall for a majority of California west of the Sierra Nevada. A reason for this may be because the ERA-Interim Reanalysis grid is much coarser than the GFS 0.5 degree, and it cannot accurately represent smaller terrain details along the coast. For the entire event rainfall accumulation time series, the 3DVAR cycling simulation had the least MAE for the north central Coastal Range HMT sites, and 3DVAR cycling experiment with ERA-Interim showed the least MAE for the windward Sierra Nevada sites. The assimilation of the COSMIC soundings appears to be beneficial for precipitation forecasts here especially for the north central Coastal Range HMT sites. In terms of the precipitation forecasts at the end of the event, the WRF-GFS experiments of surface observation nudging and the 3DVAR cycling gave the least error for the north central Coastal Range and the windward Sierra Nevada, respectively.

Future WRF experiments that focus on short-to-medium range mesoscale QPF improvement for ARs should apply observation nudging or 3DVAR at time intervals or cycling intervals less than 3 h. Using a 3-h frequency is not sufficient, and it only showed skill after 2.5 days of forecast time. Future FDDA nudging experiments should be performed without applying grid nudging directly on the inner domains, especially for such a fine inner domain of 3 km horizontal resolution. Also, more tests can be done on using different observation nudging factor values to determine which ones will lead to better QPF results. Additionally, rather than applying observation nudging throughout the entire forecast, the effectiveness of a 6- or 12-h nudging pre-forecast initialization period should be tested with a much finer nudging time step interval to include more frequent observations. As always, including a larger network of reliable surface

observations, more soundings and COSMIC GPS RO profiles, and more coastal observational datasets would only improve the data assimilation experiment results. Lastly, different data assimilation methods other than 3DVAR and FDDA nudging can also be used in WRF. For example, other WRF data assimilation methods include true 4D-Variational Analysis (4DVAR), 3DVAR's first-guess at appropriate time (FGAT) approach, and Ensemble Transform Kalman Filtering (ETKF).

References

Anthes, R.A., and Coauthors, 2008: The COSMIC/FORMOSAT-3 mission: early results. *Bull. Amer. Meteor. Soc.*, **89**, 313–333.

Baldwin, M.E., and K.E. Mitchell, 1996: The NCEP hourly multisensory U.S. precipitation analysis. *11th Conf. on Numerical Weather Prediction*, Norfolk, VA, Amer. Meteor. Soc., J95-J96.

Barker, D. M., W. Huang, Y.-R. Guo, A. J. Bourgeois, and Q. N. Xiao, 2004: A three-dimensional variational data assimilation system for MM5: implementation and initial results. *Mon. Wea. Rev.*, **132**, 897–914.

Chin, H.-N. S., P. M. Caldwell, and D. C. Bader, 2010: Preliminary study of California wintertime model wet bias. *Mon. Wea. Rev*., **138**, 3556–3571.

Colle, B. A., and C. F. Mass, 2000: The 5–9 February 1996 flooding event over the Pacific Northwest: sensitivity studies and evaluation of the MM5 precipitation forecasts. *Mon. Wea. Rev.*, **128**, 593–617.

Cucurull, L., J.C. Derber, R. Treadon, and R. J. Purser, 2007: Assimilation of Global Positioning System Radio Occultation Observations into NCEP's Global Data Assimilation System. *Mon. Wea. Rev.*, **135**, 3174–3193.

Dee, D. P., and Coauthors, 2011: The ERA-Interim reanalysis: configuration and performance of the data assimilation system. *Q. J. R. Meteorol. Soc*., **137**, 553-597.

Dettinger, M. D., F. M. Ralph, T. Das, P.J. Neiman, and D. R. Cayan, 2011: Atmospheric rivers, floods and the water resources of California. *Water*, **3**, 445-478.

Dudhia, J., 2014: WRF Four-Dimensional Data Assimilation (FDDA): WRF Tutorial, NCAR, Boulder, Colorado, January, 2014. [Available online at http://www.mmm.ucar.edu/wrf/users/tutorial/201401/WRF_FDDA_Dudhia.pdf]

Garvert, M. F., B. A. Colle, and C. F. Mass, 2005: The 13–14 December 2001 IMPROVE-2 event. part I: synoptic and mesoscale evolution and comparison with a mesoscale model simulation. *J. Atmos. Sci.*, **62**, 3474–3492.

Hahn, R. S., and C. F. Mass, 2009: The impact of positive-definite moisture advection and low-level moisture flux bias over orography. *Mon. Wea. Rev*., **137**, 3055–3071.

Hapke, C. J., 2005: Estimation of regional material yield from coastal landslides based on historical digital terrain modeling. *Earth Surf. Process. Landforms*, **30**, 679-697.

Hong, S., Y. Noh, and J. Dudhia, 2006: A new vertical diffusion package with an explicit treatment of entrainment Processes. *Mon. Wea. Rev.*, **134**, 2318–2341.

Huang, H., 2014: Introduction to WRFDA. WRF Tutorial, NCAR, Boulder, Colorado, January, 2014. [Available online at http://www.mmm.ucar.edu/wrf/users/tutorial/201401/WRFDA_Intro.pdf].

Hughes, M., P. J. Neiman, E. Sukovich, and F. M. Ralph, 2012: Representation of the Sierra Barrier Jet in 11 years of a high-resolution dynamical reanalysis downscaling compared with long-term wind profiler observations. *J. Geophys. Res*., **117**, D18116.

Jankov, I., P. J. Schultz, C. J. Anderson, and S. E. Koch, 2007: The impact of different physical parameterizations and their interactions on cold season QPF in the American River Basin. *J. Hydrometeor*, **8**, 1141–1151.

Kingsmill, D. E., and Coauthors, 2013: Kinematic and thermodynamic structures of Sierra Barrier Jets, overrunning atmospheric rivers during a land-falling winter storm in northern California. *Mon. Wea. Rev.*, **141**, 2015–2036.

Kuo, Y.-H., S. Sokolovskiy, R. Anthes, and F. Vandenberghe, 2000: Assimilation of GPS radio occultation data for numerical weather prediction. *Terres. Atmos. Oceanic Sci.*, **11(1)**, 157-186.

Lin, Y.-L., S. Chiao, T.-A. Wang, M. L. Kaplan, and R. P. Weglarz, 2001: Some common ingredients for heavy orographic rainfall. *Wea. Forecasting*, **16**, 633–660.

Liu, Y., and co-authors, 2005: Implementation of observation-nudging based FDDA into WRF for supporting ATEC test operations. 2005 WRF Users Workshop, Boulder, Colorado, June, 2005.

Ma, Z., Y.-H. Kuo, F. M. Ralph, P. J. Neiman, G. A. Wick, E. Sukovich, and B. Wang, 2011: Assimilation of GPS radio occultation data for an intense atmospheric river with the NCEP Regional GSI System. *Mon. Wea. Rev*., **139**, 2170–2183.

Marwitz, J. D., 1987: Deep orographic storms over the Sierra Nevada. Part I: Thermodynamic and kinematic structure. *J. Atmos. Sci*., **44**, 159–173.

Neiman, P. J., F. M. Ralph, A. B. White, D. E. Kingsmill, and P. O. G. Persson, 2002: The statistical relationship between upslope flow and rainfall in California's coastal mountains: observations during CALJET. *Mon. Wea. Rev.*, **130**, 1468–1492.

———, P. O. G. Persson, F. M. Ralph, D. P. Jorgensen, A.B. White, and D. E. Kingsmill, 2004: Modification of fronts and precipitation by coastal blocking during an intense landfalling winter storm in Southern California: observations during CALJET. *Mon. Wea. Rev*., **132**, 242-273.

———, F. M. Ralph, G. A. Wick, J. D. Lundquist, and M. D. Dettinger, 2008: Meteorological characteristics and overland precipitation impacts of atmospheric rivers affecting the West Coast of North America based on eight years of SSM/I satellite observations. *J. Hydrometeor.*, **9**, 22–47.

———, L. J. Schick, F. M. Ralph, M. Hughes, and G. A. Wick, 2011: Flooding in western Washington: The connection to atmospheric rivers. *J. Hydrometeor.,* **12**, 1337–1358.

Newell, R.E., N. E. Newell, Y. Zhu, and C. Scott, 1992: Tropospheric rivers? A pilot study. *Geophys. Res. Lett.*, **19**, 2401-2404.

NOAA, cited 2014: NOAA's Hydrometeorology Testbed: Overview. [Available online at hmt.noaa.gov/about/].

NCDC, 2012: Storm data and unusual weather phenomenon with late reports and corrections. Asheville, North Carolina, National Oceanic and Atmospheric Administration, National Climatic Data Center. **54**, Issue 11.

Northrop Grumman, 2002: Algorithm and data user manual (ADUM) for the Special Sensor Microwave Imager/Sounder (SSMIS). Technical Report, 1-65.

Pattantyus, A., 2011: Optimizing strategies for an observation-nudging-based four-dimensional data assimilation forecast approach with WRF-ARW. *Science and Engineering Apprenticeship Program*, Adelphi, Maryland.

Ralph, F. M., and M. D. Dettinger, 2012: Historical and national perspectives on extreme west coast precipitation associated with atmospheric rivers during December 2010. *Bull. Amer. Meteor. Soc*., **93**, 783–790.

———, and Coauthors, 2003: The impact of a prominent rain shadow on flooding in California's Santa Cruz Mountains: A CALJET case study and sensitivity to the ENSO cycle. *J. Hydrometeor*., **4**, 1243–1264.

——, P. J. Neiman, and G. A. Wick, 2004: Satellite and CALJET aircraft observations of atmospheric rivers over the eastern North-Pacific Ocean during the El Niño winter of 1997/98. *Mon. Wea. Rev*., **132**, 1721–1745.

——, ——, and R. Rotunno, 2005: Dropsonde observations in low-level jets over the northeastern Pacific Ocean from CALJET-1998 and PACJET-2001: Mean vertical-profile and atmospheric-river characteristics. *Mon. Wea. Rev.*, **133**, 889–910.

——, P. J. Neiman, G. A. Wick, S. I. Gutman, M. D. Dettinger, D. R. Cayan, and A. B. White, 2006: Flooding on California's Russian River: role of atmospheric rivers. *Geophys. Res. Lett*., **33**, L13801, doi:10.1029/2006GL026689.

Reeves, H. D., and Y. L. Lin, 2008: Dynamic forcing and mesoscale variability of heavy precipitation events over the Sierra Nevada mountains. *Mon. Wea. Rev*., **136**, 62-77.

Richard, E. and Coauthors, 2005: Quantative precipitation forecasting in mountains regions — pushed ahead by MAP. *Croat. Meteorol. J*., **40**, 65–69.

Routray, A., K. K. Osuri, and M. A. Kulkarni, 2012: A comparative study on performance of analysis nudging and 3DVAR in simulation of a heavy rainfall event using WRF modeling system. *ISRN Meteorology.* **2012**. 1-12.

Skamarock, W.C., and Coauthors, 2008: A description of the Advanced Research WRF version 3. NCAR Tech Note NCAR/TN-475+STR, 113 pp. [Available online at www.mmm.ucar.edu/wrf/users/docs/arw_v3.pdf].

Smith, B. L., S. E. Yuter, P. J. Neiman, and D. E. Kingsmill, 2010: Water vapor fluxes and orographic precipitation over northern California associated with a land-falling atmospheric river. *Mon. Wea. Rev*., **138**, 74–100.

Stauffer, D. R., and N. L. Seaman, 1994: Multiscale four-dimensional data assimilation. *J. Appl. Meteor.*, **33**, 416–434.

Thompson, G., R. M. Rasmussen, and K. Manning, 2004: Explicit forecasts of winter precipitation using an improved bulk microphysics scheme. part I: description and sensitivity analysis. *Mon. Wea. Rev.*, **132**, 519–542.

Wick, G. A., Y.-H. Kuo, F. M. Ralph, T.-K. Wee, and P.J. Neiman: 2008 Intercomparison of integrated water vapor retrievals from SSM/I and COSMIC. *Geophys. Res. Lett.* **35**, L21805.

Wentz, F. J., 1997: A well-calibrated ocean algorithm for Special Sensor Microwave/Imager, *J. Geophys. Res*., **102**, 8703–8718.

World Meteorological Organization (2010) Manual on the Global Data-processing and Forecasting System: Volume I—Global Aspects, WMO-No. 485. Geneva, Switzerland.

Yu, W., Y. Liu, and T. Warner, 2007: An evaluation of 3DVAR, nudging-based FDDA, and a hybrid scheme for summer convection forecasts using the WRF-ARW model. *18th Conf. on Numerical Weather Prediction*, 25-29 June 2007, Park City, Utah. P2.8.

Zhu, Y., and R. E. Newell, 1998: A proposed algorithm for moisture fluxes from atmospheric rivers. *Mon. Wea. Rev.*, **126**, 725–735.

APPENDIX A

Acronyms

AR	Atmospheric River
AGL	Above ground level
CAL-JET	California Land-falling Jet Experiment
CDAAC	COSMIC Data Analysis and Archive Center
CHAMP	Challenging Minisatellite Payload
COSMIC	Constellation Observing System for Meteorology Ionosphere and Climate
D1	Domain 1
D2	Domain 2
ECMWF	European Center for Medium range Weather Forecasting
EnKF	Ensemble Kalman Filtering
ERA	ECMWF Reanalysis
ESRL	Earth System Research Laboratory
ETKF	Ensemble Transform Kalman Filtering
FDDA	Four-Dimensional Data Assimilation
FGAT	First-Guess at Appropriate Time
FORMOSAT	FORMOsa Satellite
GIS	Geographic Information Systems
GPS	Global Positioning System
GPS/MET	Meteorological application of the United States Air Force GPS satellites

HMT	Hydrometeorology Testbed
IWV	Integrated Water Vapor
LEO	Low-Earth Orbiting satellite
LLJ	Low-level Jet
MAE	Mean Absolute Error
ML	Mid-Latitude
NARR	North American Regional Reanalysis
NCEP	National Centers for Environmental Prediction
NOAA	National Oceanic and Atmospheric Administration
N-S	North-South
NWS	National Weather Service
OBSGRID	Objective Analysis/Grid program for WRF
PAC-JET	Pacific Land-falling Jets Experiment
QPF	Quantitative Precipitation Forecast
RAOB	Radiosonde Observation
RIN	Radius of Influence
RO	Radio Occultation
SSMIS	Special Sensor Microwave Imager Sounder
UCAR	University Corporation for Atmospheric Research
UTC	Universal Time Coordinate system
W-E	West-East
WRF	Weather Research and Forecasting model

WRF-ARW	Advanced Research WRF
WRFDA	WRF Data Assimilation package
3DVAR	Three-Dimensional Variational Analysis
4DVAR	Four-Dimensional Variational Analysis
3-D	Three-Dimensional

APPENDIX B

HMT Station and NWS Station Information

California HMT Stations						
ID	Name	Rain Gauge ? (Y/N)	Lat.	Lon.	Elevation (msl)	Variables Assimilated*
ata	Alta	Y	39.2	-120.82	1085	*t,rh*
bbd	Big Bend	Y	39.3	-120.52	1739	*t,rh,ws,wdir*
bkr	Baker(P618)	N	35.142	-116.104	258	*t,rh,ws.wdir*
blu	Blue Canyon	Y	39.28	-120.71	1610	*t,rh,ws,wdir*
brg	Burnt Ridge	Y	38.67	-123.23	240	*t,rh,ws,wdir*
cco	Chico	Y	39.69	-121.91	41	*t,rh,ws,wdir*
ccy	CedarCyn(P298)	N	36.02	-120.3	50	*t,rh,ws,wdir*
cfx	Colfax	Y	39.09	-120.95	644	*t,rh*
cmn	Camino	Y	38.735	-120.664	1003	*t,rh*
cna	Carona	N	33.858	-117.609	300	*t,rh,ws,wdir*
cnh	Canada Hill	Y	39.18	-120.53	2020	*t,rh*
cpk	Cooke Peak(P534)	Y	37.06	-122.24	238	*t,rh,ws,wdir*
crn	Corning(P344)	Y	39.929	-122.028	50	*t,rh,ws,wdir*
czc	Cazadero	Y	38.61	-123.22	475	*t,rh,ws,wdir*
dvs	Davis	Y	38.58	-121.86	30	*t,rh,ws,wdir*
ffm	Finch Farms(P268)	Y	38.47	-121.65	7	*t,rh,ws,wdir*
fhl	Forest Hill	Y	39.04	-120.8	1042	*t,rh,ws,wdir*
gks	Greek Store	Y	39.08	-120.56	1728	*t,rh,ws,wdir*
hbg	Healdsburg	Y	38.65	-122.87	62	*t,rh*
hbk	Hornbrook	Y	41.9043	-122.5693	715	*t,rh*
hcp	Happy Camp	Y	41.79	-123.39	366	*t,rh*
hld	Hopland	Y	39.0	-123.12	165	*t,rh*
hys	Huysink	Y	39.28	-120.52	2011	*t,rh*
klm	Klamath(P316)	Y	41.559	-124.086	324	*t,rh,ws,wdir*
knv	Kernville	Y	35.754	-118.419	802	*t,rh*
lcd	Lacrosse Drive (P217)	Y	37.1	-121.65	105	*t,rh,ws,wdir*
lgt	Legget(P315)	Y	39.864	-123.717	258	*t,rh,ws,wdir*
log	Llano Grand(P174)	N	36.3	-121.05	403	*t,rh,ws,wdir*
lsn	Lake Sonoma	Y	38.72	-123.05	398	*t,rh*
lso	Los Osos	N	35.3	-120.86	1075	*t,rh,ws,wdir*
mck	Mills Creek	Y	37.47	-122.36	466	*t,rh,ws,wdir*
mhl	MeachumLfl(P196)	Y	38.3	-122.74	122	*t,rh,ws,wdir*
mta	Mendota(P304)	Y	36.74	-120.4	50	*t,rh,ws,wdir*

ndn	Norden	Y	39.32	-120.37	2100	*t,rh*
nvc	Nevada City	Y	39.385	-120.978	1055	*t,rh*
ocr	Onion Creek	Y	39.27	-120.36	1886	*t,rh,ws,wdir*
omm	Old Mammoth (P630)	Y	37.61	-119	2765	*t,rh,ws,wdir*
ons	O'Neals	Y	37.204	-119.57	693	*t,rh*
ovl	Oroville	Y	39.53	121.42	114	*t,rh*
pan	Point Arena(P059)	Y	38.93	-123.73	21	*t,rh,ws,wdir*
pfd	Pine Flat Dam	Y	36.83	-119.31	184	*t,rh*
pld	Planada(P305)	Y	37.35	-120.2	128	*t,rh,ws,wdir*
ppb	Pt. Piedras Blancas	Y	35.66	-121.29	11	*t,rh,ws,wdir*
prv	Porterville(P056)	Y	36.03	-119.06	133	*t,rh,ws,wdir*
ptv	Potter Valley	Y	39.336	-123.138	303	*t,rh*
rod	Rio Nido	Y	38.51	-122.96	30	*t,rh*
ser	SJExpRange(P725)	Y	37.09	-119.75	361	*t,rh,ws,wdir*
sms	Somis(P729)	Y	34.263	-119.096	121	*t,rh,ws,wdir*
smt	Slate Mt.(P140)	Y	38.83	-120.69	1105	*t,rh,ws,wdir*
sns	San Nicolas Island	Y	33.28	-119.52	15	*t,rh,ws,wdir*
spd	Sugar Pine	Y	39.13	-120.8	1066	*t,rh,ws,wdir*
std	Shasta Dam	N	40.72	-122.43	183	*t,rh*
sth	St. Helena	Y	38.5545	-122.485	135	*t,rh,ws,wdir*
str	Santa Rosa	Y	38.51	-122.8	40	*t,rh,ws,wdir*
svc	Sibley Volcano(P224)	Y	37.86	-122.22	439	*t,rh,ws,wdir*
tbt	Talbot	N	39.19	-120.38	1780	*t,rh*
tpk	Three Peaks	Y	35.85	-121.31	1021	---
wcc	Wild Creek(P306)	Y	37.8	-120.64	113	*t,rh,ws,wdir*
wdc	Ward Creek	Y	39.14	-120.2	2012	*t,rh*
wls	Willits	Y	39.796	-123.317	585	*t,rh*

*p=pressure, t=temperature, rh=relative humidity, ws=wind speed, wdir=wind direction. *t* and *rh* are measured at 2-m AGL. Winds are measured at 10-m AGL.

NWS Stations						
ID	Name	State	Lat.	Lon.	Elevation (msl)	Variables Assimilated*
KOAK	Oakland	CA	37.73	-122.21	3	*t,rh,ws,wdir*
KVBG	Vandenburg AFB	CA	34.75	-120.56	121	*t,rh,ws,wdir*
KREV	Reno	NV	39.56	-119.80	1516	*t,rh,ws.wdir*
KMFR	Medford	OR	42.36	-122.86	405	*t,rh,ws,wdir*

**p*=pressure, *t*=temperature, *rh*=relative humidity, *ws*=wind speed, *wdir*=wind direction